Extreme Lake-Effect Snow from a GPM Microwave Imager Perspective: Observational Analysis and Precipitation Retrieval Evaluation

LISA MILANI,[a,b] MARK S. KULIE,[c] DANIELE CASELLA,[d] PIERRE E. KIRSTETTER,[e,f] GIULIA PANEGROSSI,[d] VELJKO PETKOVIC,[a,g] SARAH E. RINGERUD,[a,b] JEAN-FRANÇOIS RYSMAN,[h] PAOLO SANÒ,[d] NAI-YU WANG,[a] YALEI YOU,[a] AND GAIL SKOFRONICK-JACKSON[i]

[a] *Earth System Science Interdisciplinary Center, University of Maryland, College Park, College Park, Maryland*
[b] *NASA Goddard Space Flight Center, Greenbelt, Maryland*
[c] *NOAA/NESDIS/STAR/Advanced Satellite Products Branch, Madison, Wisconsin*
[d] *Institute of Atmospheric Sciences and Climate, National Research Council, Rome, Italy*
[e] *University of Oklahoma, Norman, Oklahoma*
[f] *National Oceanic and Atmospheric Administration, Norman, Oklahoma*
[g] *Cooperative Institute for Satellite Earth System Studies, University of Maryland, College Park, College Park, Maryland*
[h] *Laboratoire de Météorologie Dynamique, École Polytechnique, CNRS, Palaiseau, France*
[i] *National Aeronautics and Space Administration, Washington, D.C.*

(Manuscript received 4 May 2020, in final form 25 November 2020)

ABSTRACT: This study focuses on the ability of the Global Precipitation Measurement (GPM) passive microwave sensors to detect and provide quantitative precipitation estimates (QPE) for extreme lake-effect snowfall events over the U.S. lower Great Lakes region. GPM Microwave Imager (GMI) high-frequency channels can clearly detect intense shallow convective snowfall events. However, GMI Goddard Profiling (GPROF) QPE retrievals produce inconsistent results when compared with the Multi-Radar Multi-Sensor (MRMS) ground-based radar reference dataset. While GPROF retrievals adequately capture intense snowfall rates and spatial patterns of one event, GPROF systematically underestimates intense snowfall rates in another event. Furthermore, GPROF produces abundant light snowfall rates that do not accord with MRMS observations. Ad hoc precipitation-rate thresholds are suggested to partially mitigate GPROF's overproduction of light snowfall rates. The sensitivity and retrieval efficiency of GPROF to key parameters (2-m temperature, total precipitable water, and background surface type) used to constrain the GPROF a priori retrieval database are investigated. Results demonstrate that typical lake-effect snow environmental and surface conditions, especially coastal surfaces, are underpopulated in the database and adversely affect GPROF retrievals. For the two presented case studies, using a snow-cover a priori database in the locations originally deemed as coastline improves retrieval. This study suggests that it is particularly important to have more accurate GPROF surface classifications and better representativeness of the a priori databases to improve intense lake-effect snow detection and retrieval performance.

KEYWORDS: Lake effects; Snowbands; Snowfall; Microwave observations; Remote sensing; Bayesian methods

1. Introduction

Satellite remote sensing of precipitation is essential for science and society. With global precipitation estimates available from spaceborne platforms, it becomes feasible to assess water resources, monitor extreme events, and to gain and enhance scientific knowledge regarding precipitation processes at global, regional, and smaller scales (Adler et al. 2009; Kirschbaum et al. 2017; Reed et al. 2015; Skofronick-Jackson et al. 2017; Sorooshian et al. 2011). Liquid rain precipitation has been estimated from satellites for more than five decades with accuracy improving over time (Tang et al. 2020). However, concerted efforts to estimate falling snow from spaceborne platforms have only been undertaken in the last 1–2 decades (Casella et al. 2017; Kongoli et al. 2003; Kulie and Bennartz 2009; Meng et al. 2017; Rysman et al. 2019; Skofronick-Jackson et al. 2004, 2019). Retrieving snowfall from space is necessary to globally quantify water resources transported from the atmosphere to land surfaces. However, developing accurate falling snow estimates has been challenging because of snowflake particle complexities (Gong and Wu 2017; Kneifel et al. 2020; Liu and Seo 2013; Skofronick-Jackson and Johnson 2011), frozen surface contamination of the snowflakes scattering signature (Ebtehaj and Kummerow 2017; Prigent et al. 2006), and nonlinear relationships between observations and the retrieved products.

The Global Precipitation Measurement mission (GPM; Hou et al. 2014; Skofronick-Jackson et al. 2017), an ongoing NASA earth system science mission, is dedicated to quantifying precipitation on a near-global basis. The GPM *Core Observatory* (GPM-CO) was launched in 2014 with the Dual-Frequency

Corresponding author: Lisa Milani, lisa.milani@nasa.gov

DOI: 10.1175/JTECH-D-20-0064.1

Precipitation Radar (DPR; Iguchi 2020; Toyoshima et al. 2015) and the GPM Microwave Imager (GMI; Draper et al. 2015; Wentz and Draper 2016) on board. The GPM-CO flies on a non-sun-synchronous orbit (65° inclination angle), allowing precipitation retrievals up to the Arctic and Antarctic Circles. Detecting snowfall is one of the critical GPM mission requirements. Both DPR and GMI have shown snowfall detection capabilities (Adhikari et al. 2018; Casella et al. 2017; Ebtehaj and Kummerow 2017; Panegrossi et al. 2017; Rysman et al. 2018; You et al. 2017; Petersen et al. 2020). However, different sampling strategies, sensor sensitivities, phase classification, and other algorithm assumptions strongly influence global snowfall detection statistics (Skofronick-Jackson et al. 2019). In particular, the Goddard Profiling Algorithm (GPROF; Kummerow et al. 1996; Kummerow et al. 2015), which retrieves precipitation rates using passive microwave (PMW) observations, generally underestimates both snowfall detection and quantification when compared to active remote sensing sensor snowfall products. Previous studies based on theoretical analyses (Skofronick-Jackson and Johnson 2011) and radiometer observations (Panegrossi et al. 2017; You et al. 2017) showed that low-frequency channels (10–37 GHz) contain limited snow detection information compared to higher frequencies (89–183 GHz). In contrast, the channels at 183.31 ± 3, 183.31 ± 7, and 166 GHz are respectively more important because of their sensitivity to frozen hydrometeors and increasing ability to travel through the atmosphere to sense shallow events, especially for low total precipitable water (TPW) conditions. Numerous previous studies have demonstrated the potential of the use of observed brightness temperature (TB) differences in channel pairs with weighting functions that peak at different atmospheric levels (e.g., 183.31-GHz band channels) for snowfall detection and retrieval (e.g., Kongoli et al. 2015). On the other hand, the 166-GHz polarization signal is also analyzed, since it can provide impactful information content for snowfall detection also at higher latitudes (e.g., Gong and Wu 2017; Panegrossi et al. 2017).

Satellite-based snowfall detection performance can also be influenced by snowfall regimes, with intense, deeper events accompanied by higher columnar water vapor amounts typically easier to detect than light and/or shallow snowfall events that occur in drier ambient conditions (e.g., Skofronick-Jackson et al. 2013). Several recent studies highlight different snowfall modes both from satellite (Kulie and Milani 2018; Kulie et al. 2016; West et al. 2019; Kulie et al. 2020) and ground-based radar perspectives (Pettersen et al. 2018; Pettersen et al. 2020). Deeper cloud structures that are characteristic of midlatitude winter cyclones are generally easier for PMWs to detect due to strong scattering signals from ice particles and higher reflectivity values that can be detected by radars with reduced sensitivity. Shallow snowfall, however, presents unique PMW detection complexities at higher latitudes since its radiative signal can be difficult to discern over snow-covered surfaces. Depending on radar sensitivity and near-surface blind zone extent, spaceborne radars might also not detect shallow snow events because of lighter radar reflectivities and extremely shallow cloud tops (Maahn et al. 2014; Pettersen et al. 2020).

Compounding potential detection difficulties, shallow convective snow has important hydrological, ecological, and socioeconomic impacts. Lake-effect snow (LES) is a form of shallow convective snow produced during cold-air outbreaks, whereby cold air interacts with unfrozen or partially frozen bodies of water. Shallow, lake-induced convection can persist over the same area for days, accumulating large amounts of snow over neighboring land regions. This snowfall mode commonly occurs in the U.S. Great Lakes region. Several studies have covered this topic from a ground-based or numerical model perspective (Liu and Moore 2004; Notaro et al. 2013; Scott and Huff 1996; among others). Scott and Huff (1996), for example, demonstrated that precipitation amount during winter can be 50% higher downwind of Lakes Ontario or Erie and up to 100% higher over the eastern shore of Lake Superior compared to what is expected without the contribution of LES. Pettersen et al. (2020) showed almost 80% occurrence and 50% contribution to annual snowfall accumulation in the upper Great Lakes. Analyzing the past 6 winter seasons (2014–20), on average 10 intense LES events [identified by the NWS (2020) in their "Lake-effect snow event archive"], affect the lower Great Lakes region every year, with an average total yearly accumulation of 405 cm (with a mean 24 h accumulation of 28 cm) for Lake Erie and 615 cm (with a mean 24 h accumulation of 47 cm) for Lake Ontario. Spaceborne radar datasets also highlight LES prevalence globally with distinct seasonal cycles and notable shallow convective maxima located over extended high-latitude oceanic regions (Kulie and Milani 2018; Kulie et al. 2016, 2020). The Kulie et al. (2016) and Kulie and Milani (2018) *CloudSat* studies showed that 36% of snowfall events and 18% of snowfall amount are globally related to shallow convective events and they can increase to over 50% of the annual estimated surface snowfall flux on a regional scale.

However, surface temperatures and columnar water vapor levels associated with LES are usually very low (e.g., < 5 mm), with low water vapor amounts portending potential PMW detection difficulties. For instance, Panegrossi et al. (2017) analyzed parameters influencing the 166-GHz polarization difference and found that snowfall detection over land becomes problematic when TPW is below 3.6 mm.

Further PMW studies dedicated specifically to shallow convective snow are currently lacking. This work therefore focuses on intense [defined by Notaro et al. (2013) and Liu and Moore (2004) as events with 24 h snow accumulation >10 cm] shallow convective snowfall event detection and quantification from PMW observations over the U.S. Great Lakes region. The availability of an operational ground-based radar network over the region makes it the perfect test bed for comparing GPROF precipitation retrievals to the GPM Ground Validation Multi-Radar Multi-Sensor (GV-MRMS; Kirstetter et al. 2018). The specific motivational questions of this study are as follows:

- Do distinctive multifrequency passive microwave brightness temperature signals accompany intense LES events?
- How does GPROF perform for these extreme snow-producing events?
- What factors affect GPROF performance?

- What algorithm components can be improved to mitigate potential shortcomings?

In particular, this study presents two extreme LES cases over the lower Great Lakes region, with National Weather Service (NWS) reported measured accumulation of about 124 cm in 24 h south of Buffalo, New York, for the first case study and about 140 cm (103 cm in 24 h) downwind of Lake Ontario for the second case, showing hourly accumulation 1.2–3.5 times the average hourly accumulation of intense LES events that occur over the region.

The next section introduces the sensors used in this study and the characteristics of the GPROF algorithm, followed by a description of the GV-MRMS ground evaluation dataset. The two extreme LES events and accompanying GPM/GV-MRMS analyses are presented in section 3. Section 4 focuses on results and recommendations to improve GPROF retrievals. The paper ends with a discussion and concluding remarks.

2. Data and products

GPM-CO is the central component of a constellation of research and operational satellites built with several international collaborators. It orbits at an altitude of 407 km and carries the GMI and DPR. The GMI is a conical scanning radiometer with a swath of 880 km. It is outfitted with 13 channels from 10.65 to 183.1 ± 7 GHz, with spatial resolutions spanning from 32.1 km × 19.4 km for the low-frequency channels to 5.8 km × 3.8 km for the high-frequency channels (Draper et al. 2015). The availability of high-frequency channels (166-GHz V-pol and H-pol and 183.31 ± 3- and 183.31 ± 7-GHz V-Pol) provides valuable information about snowfall given their high ice/snow scattering sensitivity. Together with GMI, the GPM-CO carries the first dual-frequency precipitation radar. Although DPR products are not directly used in this study, the a priori GPROF database built using DPR and other instrument precipitation estimates constitutes a crucial component of the present work. DPR characteristics are described in detail in section 2c.

a. GPROF retrieval algorithm

The GPROF algorithm (Kummerow et al. 1996, 2001, 2015; Meyers et al. 2015) serves as the operational precipitation retrieval for the GPM PMW sensor constellation. This scheme estimates the probability of precipitation relying on a Bayesian approach using an a priori knowledge (i.e., an a priori probability) to link the TB vector and occurring atmospheric state. The a priori knowledge is stored in a so-called a priori database, enabling easy access to previously established links between TBs and corresponding precipitation rates. GPROF relies on these links to form a weighted mean of the database precipitation rate using the difference between the a priori and observed TB elements to construct the appropriate weights. Details on the Bayesian theory can be found in Rodgers (2000), while further details about GPROF's evolution are presented in Kummerow et al. (1996, 2001, 2015) and Meyers et al. (2015).

To ensure a robust link between surface precipitation rates and corresponding radiative signatures at the top of the atmosphere, the version-5 (V5) operational a priori database relies on version-4 (V4) DPR Ku precipitation retrievals over vegetated surfaces, inland waters, and coastlines (section 2c) and on the V4 DPR-combined (CMB) algorithm (Grecu et al. 2016) over oceans, sea ice, and sea ice/ocean boundaries. The database is built with one year of GPM data (DPR and CMB), from September 2014 to August 2015. GV-MRMS (section 2b) estimates are used over snow-covered surfaces. The database is built matching two years of GV-MRMS data (from April 2014 to August 2016) with satellite overpasses. The precipitation phase is determined by GPROF [following the Sims and Liu (2015) methodology] so as to have a common classification method with the other two a priori databases (DPR and CMB based).

The mechanics behind constructing the GMI sensor a priori information include using observed TBs (Kummerow et al. 2011) and ancillary information like TPW, surface type, and 2-m temperature (T2m). The three ancillary elements partition the a priori database and constrain the TB–precipitation-rate relationship. In this process, surface types are obtained from an SSM/I-observed emissivity climatology (Aires et al. 2011) and its daily updates by NOAA's AutoSnow product (Romanov et al. 2000). GPROF can classify 14 different classes: 5 for increasing vegetated land, 4 for increasing snow-covered surfaces (minimum, low, moderate, and maximum snow cover), sea ice, ocean, standing waters, coastlines, and sea ice edge. These classes come from a cluster analysis, purely empirical self-grouping of emissivity characteristics (Prigent et al. 2006). The TPW and T2m parameters are obtained from the Global Atmospheric Analysis (GANAL; JMA 2000) and the European Centre for Medium-Range Weather Forecasts (Dee et al. 2011) reanalysis datasets for the operational and the climatological GPROF outputs, respectively.

For this study, the 1C-R-GMI product (TBs) and the climatological 2A-GPROFGMI (precipitation rates and environmental information) have been used. These datasets are freely available through the NASA Precipitation Processing System (PPS) data archive (https://storm.pps.eosdis.nasa.gov/storm/).

b. GV-MRMS

The MRMS system uses precipitation observations from the polarimetric Next Generation Weather Radars (NEXRAD) and automated rain gauge networks in the conterminous United States (CONUS) and southern Canada (Zhang et al. 2011). MRMS generates quantitative precipitation estimation (QPE) and precipitation phase products from observed radar reflectivities at a 0.01° horizontal resolution every 2 min. MRMS runs operationally at the National Centers for Environmental Prediction. Temperature and humidity analyses from the Rapid Refresh (RAP; Benjamin et al. 2004) model are used to segregate surface rain from snow. The radar QPE uncertainty depends on various factors such as beam blockage, beam height, vertical structure of precipitation, etc. (Kirstetter et al. 2015). MRMS internal procedures mitigate the impact of these factors. To quantify snow rates, MRMS uses a fixed reflectivity–snowfall rate (Z–S) relationship:

$$Z = 75S^2. \quad (1)$$

The minimum reflectivity threshold is 5 dBZ for snow (corresponding to a liquid equivalent snowfall rate of ~0.2 mm h^{-1}). A fixed Z–S relationship obviously causes uncertainties and may require modifications for LES QPE, but MRMS represents a convenient proxy for snowfall intensity. Proposed MRMS advancements will incorporate uncertainty as an integral part of QPE with probability distributions of precipitation rates (Kirstetter et al. 2015).

To derive GV-MRMS precipitation products used for satellite purposes, the 0.01°-resolution MRMS-defined precipitation pixels coincident with GPM-CO overpasses over the United States are averaged within each GPM-GMI footprint to match the larger satellite field of view (e.g., Kirstetter et al. 2012). The precipitation reference dataset is refined by conservatively filtering precipitation rates associated with radar beam height above 2.5 km above ground level in order to mitigate uncertainties in the relation between ice aloft and surface snowfall. The product just described represents the precipitation-rate reference for the GPROF a priori database over snow-covered surfaces (see section 2a). It is worth noting that the 0.2 mm h^{-1} (5 dBZ) minimum threshold is applied to the MRMS product at its native 0.01° resolution, so in the averaged GV-MRMS product matching the GPM-GMI spatial resolution, lower precipitation rates (also < 0.2 mm h^{-1}) could be found. For database purposes, the precipitation phase of GV-MRMS observations is determined by the Sims and Liu (2015) method directly within the GPROF algorithm.

Despite the uncertainties, GV-MRMS retrievals are the best available QPE dataset over CONUS and are thus used in the present study to evaluate GPROF performance. For this purpose, we use the GV-MRMS precipitation phase identification based on a RAP surface (wet bulb) temperature thresholds of 2° (0°) C. For the following analysis, a 0.1 mm h^{-1} threshold was chosen for GV-MRMS to take into account the reflectivity threshold [Eq. (1)] and the averages of GV-MRMS rates within a GPM-GMI footprint.

c. DPR

The DPR consists of Ku-band (13.6 GHz) and Ka-band (35.5 GHz) channels. The combination of the two better constrains the particle size distribution, which in return reduces the quantitative precipitation estimation uncertainties. The DPR's spatial resolution is 5 km at nadir and it scans with a 245- and 120-km swath for Ku and Ka bands, respectively. The DPR-Ku precipitation product is used to build the a priori database for vegetated surfaces, inland waters, and coastlines. With a detection threshold of 12 dBZ (Hamada and Takayabu 2016; Skofronick-Jackson et al. 2019) the instrument is capable of detecting surface precipitation rates of approximately 0.5 mm h^{-1} (Kozu et al. 2001; Kubota et al. 2016).

3. Case studies

Seven similar LES events over the lower Great Lakes region were manually selected among the common events in the Buffalo lake-effect snow archive, the GPM overpasses during the 2014–15 period and the MRMS available data. Two events with opposite behavior are analyzed in this study to possibly identify the weaknesses of GPROF on detecting and quantifying LES.

These specific cases are chosen for two reasons. First, they are both long-lived snowfall events with deeper cloud structures (~3–4-km cloud-top heights; Figs. 2b and 6b) and more extreme snowfall rates than the global population of cumuliform snow events (Kulie et al. 2016). These events therefore serve as appropriate illustrative cases to interpret multifrequency GMI signatures associated with extreme LES events. Second, both events did occur within the observational period considered in the GPROF a priori database. In particular, for the first case (orbit 4140) GV-MRMS data are included in the a priori database, while for the second case (orbit 4914) both DPR and GV-MRMS information are included. This selection criterion thus allows GPROF performance to be assessed, specifically if the algorithm can correctly convert GMI TBs into a physically realistic retrieval for this unique class of extreme winter precipitation. The analysis comprises the following components: GMI TB observational descriptions, visual comparisons of precipitation patterns, event detection and QPE assessments, statistical scores of detection ability, and a GPROF–GV-MRMS correlation (r) analysis. The statistical scores used for this analysis are the false alarm ratio (FAR), Heidke skill score (HSS), and critical success index (CSI), all based on the comparison between the actual retrieval (GPROF estimates) and a reference value (GV-MRMS in our case). Detailed description of statistical scores can be found in Nurmi (2003).

a. 20 November 2014 (GPM-CO orbit 4140)

1) GMI OBSERVATIONAL ANALYSIS

The first case study is a LES event that occurred on 20–21 November 2014 over Lakes Erie and Ontario in the lower Great Lakes region. This event formed within a cold-air outbreak behind an occluded frontal system that produced unseasonably cold temperatures. T2m ranged between ~263 and 274 K during the event, with T2m values at the higher end of this range when the GPM-CO overpassed near 1820 UTC 20 November 2014 (Fig. 1a). Upper-air observations and reanalysis datasets revealed TPW values between 4 and 5 mm on 20 November—a dry postfrontal ambient environment that is typically associated with LES events[1] (Fig. 1b). Lake Erie and Ontario surface temperatures ranged from ~7° to 12°C.[2] The relatively warm lake surfaces and cold 850-hPa temperatures (~ −12° to −14°C) produced sufficient low-level instability to initiate boundary layer convection. Postfrontal winds flowed across the long axis of the lakes to organize and sustain shallow (~3–4 km radar-indicated cloud depths; Fig. 2b), yet convectively robust, LES bands.

NEXRAD radar observations from the Buffalo (KBUF) and Fort Drum (KTYX), New York, sites near 1820 UTC

[1] Twice-daily radiosondes are launched at the Buffalo National Weather Service Weather Forecast Office (http://weather.uwyo.edu/upperair/sounding.html).

[2] Daily lake surface temperature analyses are available from the NOAA Great Lakes Environmental Research Laboratory (https://coastwatch.glerl.noaa.gov/glsea/glsea.html).

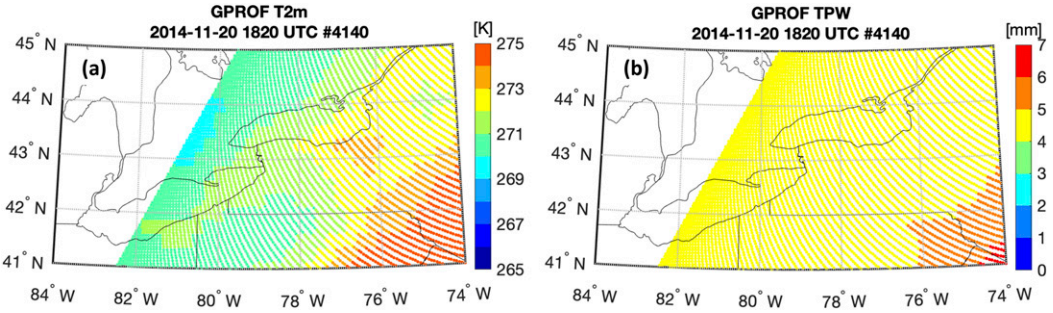

FIG. 1. ECMWF reanalysis (a) T2m and (b) TPW for the GPM-CO overpass near 1820 UTC 20 Nov 2014. T2m and TPW from ECMWF are provided as GPROF product parameters.

20 November 2014 indicated respective long lake-axis-parallel (LLAP; Steiger et al. 2013) snowbands over both Lakes Erie and Ontario with radar reflectivities exceeding 30 dBZ in the strongest convective cores (Fig. 2a). Reflectivities increased across the lakes as the cumulative effect of air/lake latent and sensible heat exchanges, combined with mesoscale influences, progressively invigorated boundary layer convective processes. Convective vigor was further confirmed by multiple lightning reports during this event. These bands persisted for almost 24 h over both lakes, producing more than 120 cm of snow accumulation south of Buffalo for the entire event duration.[3] Significant snowpack already existed over Lake Erie lake-effect snowbelt regions, the inland regions east of Lake Ontario, and the south-central Canadian Ontario province from a previous LES event (not shown). No snow cover was diagnosed over the southeast quadrant of the scene (as also shown in Fig. 4d).

Multifrequency GMI TBs are first analyzed to assess whether GMI observes distinctive radiometric signatures for this convective snow event (Fig. 3). All window channels show evidence of large land surface variability, with higher TBs in the sparsely snow-covered/vegetated southeastern portion of the domain, and lower TBs in presence of deep dry snow around the lakes. Lower-frequency GMI channels (10–37 GHz) do not typically display precipitation-related signatures for LES (Skofronick-Jackson et al. 2013). Warmer 19-, 23-, and 37-GHz TBs relative to the radiometrically cold lake surface background, however, are noted over both lakes due to liquid or mixed-phase precipitation (not shown). Similar TB emission signals are also found in 89- and 166-GHz channels over the lakes (Figs. 3a–f) as a result of cloud water emission. For instance, 89-GHz vertical (V) polarization TB (TB_{89V}) values are ~5–15 K higher over central and eastern Lake Ontario relative to surrounding cloud-free observations (Fig. 3a; red circle). $TB_{89V} - TB_{89H}$ differences (ΔTB_{89}) are also noticeably lower (~30–35 K) within overlake clouds compared to surrounding 50–60-K ΔTB_{89} values that accentuate highly polarized surface water features under clear conditions (Fig. 3c; red circle).

In addition to cloud water emission sensitivity, GMI higher-frequency (89–183.31 GHz) channels delineate likely surface snowfall regions since they are progressively more sensitive to frozen hydrometeor scattering signals. Warmer TBs from possible cloud water emission at 89 and 166 GHz evolve into distinct TB depressions (i.e., colder TBs within snowbands compared to surrounding nonsnowing observations) as cloud thickness, snow/ice particle size, integrated columnar ice paths, and surface snowfall rates increase over the eastern lake surfaces. The snowband observed by NEXRAD over eastern Lake Erie (79.5°–77.5°W) and extending inland for almost 100 km (Fig. 2) is accompanied by GMI 166-GHz TB depressions reaching ~30 K (Figs. 3d,e; red circles). Lower TB depressions are also apparent at 89 GHz. Polarization difference signatures are also noteworthy over land in the Lake Erie snowband. At 166 GHz (ΔTB_{166}) it is observed far inland (Fig. 3f; yellow circle), while at 89 GHz (ΔTB_{89}) it is only apparent near the immediate Lake Erie shoreline (Fig. 3c; yellow circle). Similar 89- and 166-GHz signals, albeit with lower TB depression magnitudes, are also evident in the NEXRAD-observed Lake Ontario snowband that extends over most of the lake and over the Tug Hill Plateau region in upstate New York (77°–74°W).

The 183.31 ± 7V- and 183.31 ± 3V-GHz channels provide further evidence that distinct GMI signals accompany this LES event. These channels offer increased ice/snow particle scattering sensitivity, but their respective locations near the 183.31-GHz water vapor absorption line typically provide information from mid- to upper-atmospheric levels and therefore might not be deemed appropriate for shallow precipitation remote sensing applications. However, very low TPW values allow 183.31-GHz weighting functions to peak at lower atmospheric levels and therefore respond to the LES bands (e.g., Edel et al. 2019). Furthermore, these channels are somewhat immune to surface-related emissions since sufficient boundary layer water vapor exists. As shown in Figs. 3g–i, significant $TB_{183.31}$ depressions correspond to the Lake Erie and Ontario snowbands. $TB_{183.31\pm7}$ depression magnitudes are larger than $TB_{183.31\pm3}$ since the 183.31 ± 7-GHz channel weighting function peaks at lower atmospheric levels (Figs. 3g,h; blue circles). $TB_{183.31\pm7}$ and $TB_{183.31\pm3}$ differences ($\Delta TB_{183.31}$) effectively isolate the LES bands, with $\Delta TB_{183.31}$ values below −15K in the most

[3] Snow accumulations reported by the Buffalo National Weather Service Weather Forecast Office.

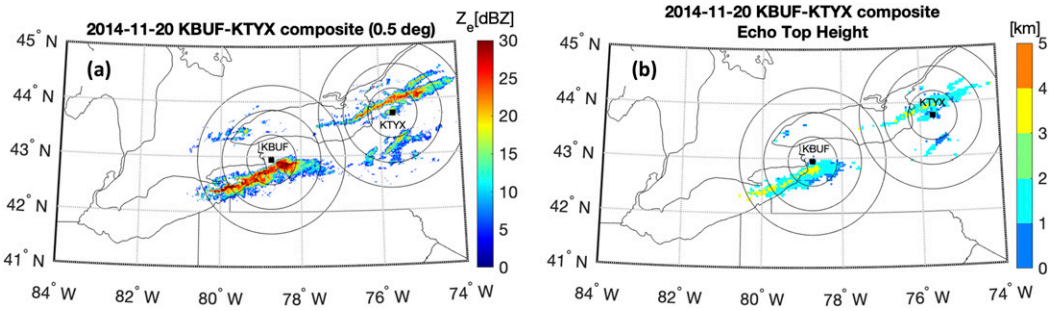

FIG. 2. NEXRAD level-III products (a) base scan composite radar reflectivity and (b) echo-top height, using data from the Buffalo (KBUF) and Fort Drum (KTYX) sites at 1818 and 1821 UTC 20 Nov 2014; 50-, 100-, and 150-km ranges are also shown.

intense snowfall locations (Fig. 3i; blue circles). Furthermore, $\Delta TB_{183.31}$ signals over land are much more distinctive than ΔTB_{89} (Fig. 3c) and ΔTB_{166} (Fig. 3f). Similar to 89- and 166-GHz analyses, the Lake Erie snowband is inferred to be more intense than the Lake Ontario snowband due to larger $\Delta TB_{183.31}$ magnitudes.

Interestingly, the collective TB observations also infer different processes operating within the respective snowbands. For instance, the Lake Erie band shows consistent scattering signals over a substantial part of the lake and over land. Conversely, significant high-frequency GMI scattering effects in the Lake Ontario snowband are only apparent over land despite elevated NEXRAD radar reflectivity values over the eastern part of the lake, thus hinting at significant land/orographic enhancements and/or overlake microphysical composition differences compared to the Lake Erie snowband. Positive $\Delta TB_{183.31}$ magnitudes elsewhere in the scene infer higher $TB_{183.31\pm7}$ values and are mostly associated with nonprecipitating or lightly precipitating observations. A few positive $\Delta TB_{183.31}$ values, however, correspond to higher precipitation rates and reflect the complicating contribution of supercooled liquid water within snowbands that dampen scattering effects (Panegrossi et al. 2017). $TB_{183.31\pm7}$ are demonstrably higher than $TB_{183.31\pm3}$ where the scene is not affected by lake-effect clouds because of the combined background surface (as in the southeastern scene quadrant) and water vapor emission. Both lakes locally increase boundary layer water vapor content, as indicated by

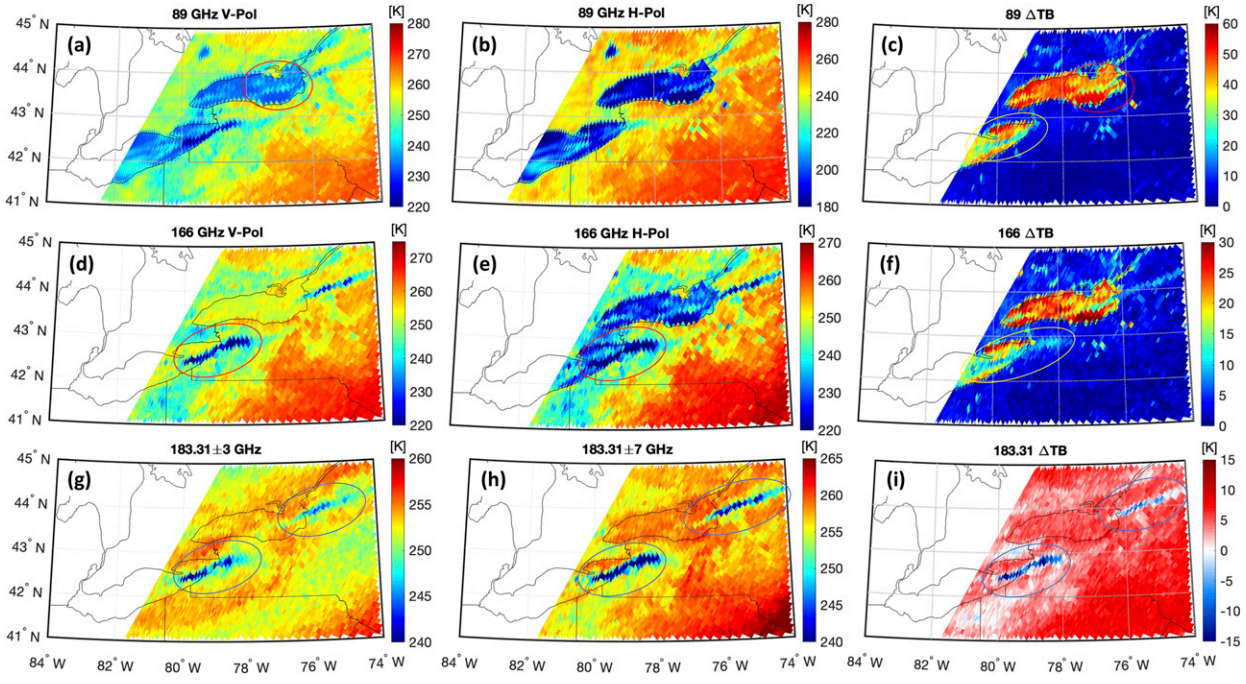

FIG. 3. GMI (a) TB_{89V}, (b) TB_{89H}, and (c) ΔTB_{89} (K) for 1820 UTC 20 Nov 2014 (GPM orbit 4140). GMI (d) TB_{166V}, (e) TB_{166H}, (f) ΔTB_{166}, (g) $TB_{183.31\pm3}$, (h) $TB_{183.31\pm7}$, and (i) $\Delta TB_{183.31}$ are also shown. Circles are added here to highlight some of the important features described in the text.

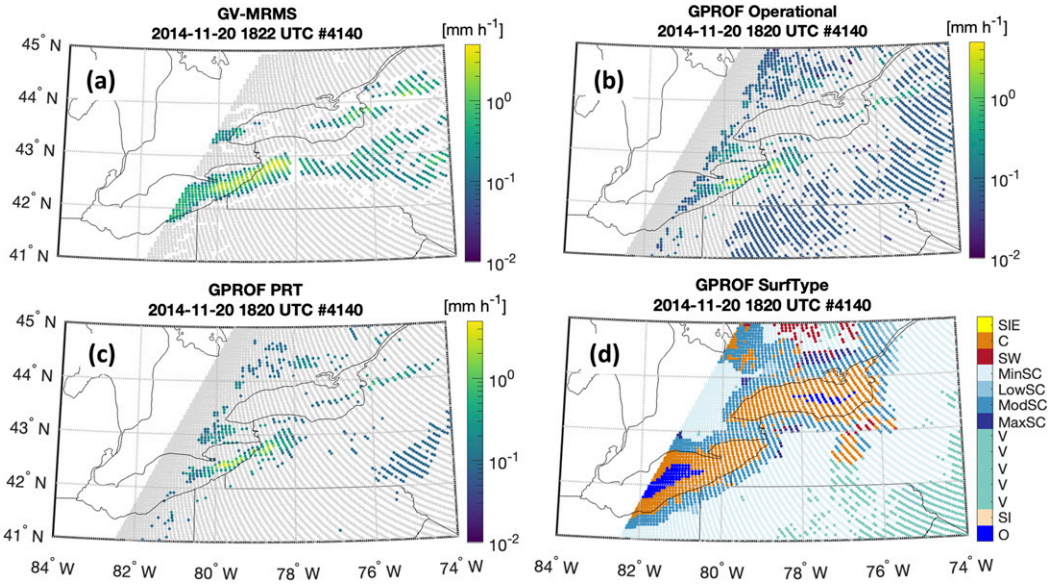

FIG. 4. (a) MRMS-GV snowfall rate over Lakes Erie and Ontario on 20 Nov 2014 at 1820 UTC (orbit 4140), (b) GPROF precipitation rate (using the SurfPrecip parameter from the operational product), (c) GPROF PRT precipitation rate ($\geq$0.08 mm h^{-1}), and (d) surface classification as from the GPROF SurfType parameter: Sea ice edge (SIE), land/ocean or water coast (C), standing water (SW), minimum snow cover (MinSC), low snow cover (LowSC), moderate snow cover (ModSC), maximum snow cover (MaxSC), vegetation (V; 5 classes), sea ice (SI), and ocean (O).

higher $TB_{183.31\pm7}$ values lake surfaces that are not significantly covered by lake-effect clouds (Fig. 3h).

2) GPROF PERFORMANCE

The previous section highlighted clear multifrequency TB signals in LES bands for the 20 November 2014 event. We then evaluated GPROF's ability to successfully detect this type of snowfall event and provide meaningful snowfall rate estimates. Figure 4 shows the surface precipitation retrievals from both GV-MRMS (Fig. 4a) and the GPROF operational algorithm (Fig. 4b). All precipitation rates are assumed to be liquid-equivalent snowfall rates since this event produced prolific snowfall totals. Moreover, reanalysis T2m (Fig. 1a) and the GPROF frozen precipitation parameter (not shown), suggest that snow is the predominant precipitation type. Lighter mixed precipitation, however, cannot be entirely discounted during the GPM-CO overpass time in shallow cloud features located over the central lakes due to possible emission signatures observed in lower-frequency channels (not shown).

GPROF clearly indicates light precipitation over non-precipitating regions according to GV-MRMS (Figs. 4a,b). It is worth reminding that GV-MRMS considers only $\geq$ 5 dBZ observations (precipitation rate $\geq$ 0.2 mm h^{-1}), but, considering beam filling issues into account in matching GMI footprint, 0.1 mm h^{-1} is considered as the minimum GV MRMS threshold. Therefore, rates below 0.1 mm h^{-1} have been filtered out in the GV-MRMS product for this analysis. Operational V5 GPROF has a lower precipitation limit of 0.01 mm h^{-1}. Furthermore, GPROF will tend to overestimate widespread light precipitation as an artifact of the Bayesian retrieval mechanics.

When compared pixel by pixel (not shown), operational GPROF and GV-MRMS show a good correlation ($r > 0.6$) above 0.1 mm h^{-1} (0.3 mm h^{-1} for GV-MRMS) although with a general underestimation shown by GPROF. Below these thresholds, GV-MRMS precipitation rates decrease till 0 mm h^{-1}, while the corresponding GPROF values are all included within the 0.06 and 0.1 mm h^{-1} interval justifying the widespread low precipitation rates shown by GPROF where GV-MRMS shows no precipitation.

Before interpreting GPROF snowfall rate estimates, we considered the algorithm quality flag (QF; introduced by the developers in V5) to analyze the precipitating pixels quality. QFs with values 0 or 1 indicate reasonable performance and are deemed usable in the analysis. QFs above 1 mean poor or indeterminate quality and developers suggest not to consider these retrievals for individual events (Passive Microwave Algorithm Team Facility 2017). Most of the light precipitating pixels are associated with QF = 2 (not shown), which is "use pixel with extreme care over snow covered surface." Following the developer suggestion, the QF = 2 pixels were at first filtered out, but this method resulted to be too conservative and lead to completely miss precipitation over land. For this reason, in an effort to improve GPROF comparisons with GV-MRMS, we decided to address the problem and offer a quick solution to users dealing with the current product version (V5), till some improvements will be implemented in future versions. We opted for a simple precipitation-rate threshold (PRT) approach (Kirstetter et al. 2014). Systematic HSS analyses

TABLE 1. Statistical scores comparing GPROF precipitation rates [operational (Op) and applying PRT] with GV-MRMS precipitation product for the two cases. The PRTs considered case by case are also shown.

		HSS		FAR		CSI		r	
	Threshold (mm h^{-1})	Op	PRT	Op	PRT	Op	PRT	Op	PRT
4140	0.08	0.09	0.26	0.77	0.57	0.18	0.23	0.65	0.61
4914	0.11	−0.01	0.11	0.80	0.54	0.16	0.10	0.43	0.51

between operational GPROF and GV-MRMS suggest a suitable PRT value of 0.08 mm h^{-1} for this event (corresponding to the best HSS score after testing all the possible precipitation thresholds from 0 to 1 mm h^{-1} at 0.01 mm h^{-1} increments). This threshold is also consistent with the 0.1 mm h^{-1} threshold applied to GV-MRMS for this study. PRT results (Fig. 4c) present a precipitation structure pattern much more similar to GV-MRMS (Fig. 4a) than the operational product (Fig. 4b). The PRT method improves all of the statistical scores, increasing the CSI (0.23) and HSS (0.26) and decreasing the FAR (0.57) relative to operational results (Table 1). GPROF false detections are still abundant, but PRT suitably comprises false detections and the risk of missing actual precipitation. The GPROF and GV-MRMS correlation index using PRT slightly decreases ($r = 0.61$) relative to the operational product ($r = 0.65$) but can still be considered a reasonable result for a PMW algorithm retrieval of solid precipitation compared to other algorithms (Meng et al. 2017; Rysman et al. 2019).

The climatological emissivity given for GPROF, combined with the AutoSnow product update, classifies the surface adjacent to Lakes Erie and Ontario as snow covered (Fig. 4d). Additionally, large areas are classified as coastline over the water and the land directly surrounding Lakes Ontario and Erie. Both snowbands are partitioned almost equally between coastline and snow-covered surfaces, thus prompting the GPROF algorithm to use both its DPR and MRMS a priori databases, respectively. One of GPROF's strengths is that it shows precipitation pattern continuity over different surface types, despite the fact that the retrieval uses different a priori conditions.

b. 9 January 2015 (GPM-CO orbit 4914)

1) GMI OBSERVATIONAL ANALYSIS

The second case considered is another extreme multiday (9–10 January 2015) LES event. Postfrontal environmental conditions were similar to the first case, albeit with colder T2m values (e.g., <263 K upwind of Lakes Erie and Ontario; Fig. 5a) and slightly lower TPW values (e.g., 3–4 mm; Fig. 5b). The January event timing and extremely cold temperatures enabled ice development over western portions of Lake Erie, but the central and eastern lake remained ice-free (not shown). Lake Ontario was also mostly ice-free, except for some nearshore locations. With optimally aligned winds interacting with sufficient open lake surfaces and 850-hPa temperatures between −15° and −23°C, LES bands developed over both lakes.

Figure 6 shows KBUF and KTYX NEXRAD observations near 1230 UTC 9 January 2015 coincident with a GPM-CO overpass. The Lake Erie snowband was oriented in a southwest–northeast direction directly over coastal land areas, while the Lake Ontario band was located mostly over water near the northern lake shoreline. The Lake Erie snowband appeared more intense (maximum reflectivities of >30 dBZ) at this juncture compared to its Lake Ontario counterpart, but total snow accumulations were much higher downwind of Lake Ontario (~140 cm) compared to Lake Erie (~60 cm). This disparity can easily be explained with the instantaneous acquisition of the radar reflectivity that could not reflect the final accumulation recorded by the NWS stations and radar precipitation accumulation products. Land surfaces in the region were entirely snow-covered, with higher snowpack values located over lake-effect snowbelt regions and over a broad swath of the Canadian Province of Ontario from recent synoptic and LES events (see Fig. 8d for GPROF surface classification).

The GPM-CO captured this event near 1226 UTC 9 January 2015 (Fig. 7). Similar to the first event, a significant TB response is noticeable for all GMI high-frequency channels. The Lake Erie snowband exhibited 20–30K TB depressions in most high-frequency channels. For instance, lower 89-GHz TBs were collocated with the snowband and were accentuated by radiometrically warmer background surface in the southeastern coastline and inland cloud-free areas (Figs. 7a,b; blue circles). Nearby cloud-free Lake Erie surfaces displayed colder and highly polarized ΔTB_{89} signals (Fig. 7c). Similar 166-GHz trends were observed over the Lake Erie snowband, but with colder TBs (Figs. 7d,e; blue circles). Unlike the 89-GHz channels, 166-GHz TB polarization differences were associated with the Lake Erie snowband over coastal land regions (Fig. 7f; yellow circle). It is worth noting the different 89- and 166-GHz TB signatures over interior Canada (northwest part of the scene; Figs. 7a,b,d,e; red circles) compared to the southeastern quadrant of the scene. There are many factors that may contribute to the lower TBs observed in the northwest portion of the domain, such as colder skin temperature (as shown by MERRA 2 reanalysis, not shown), or presence of nonprecipitating clouds (as indicated by GOES IR/VIS images and by the Canadian Exeter, Ontario, radar, not shown). However, the observed TB depression at all frequencies (including 10 and 19 GHz), and the strong polarization signal can be attributed to the snowpack properties in that region, clearly different from the southeastern portion of the domain, as evidenced by the GMI surface emissivity maps (not shown, Munchak et al. 2020). The 183.31-GHz channels also exhibited sensitivity to frozen hydrometeor scattering, with $\Delta TB_{183.31}$ values between −10 and −15 K effectively highlighting the most intensive snowfall regions (Fig. 7i; blue circles).

Similar 183.31-GHz TB attributes were collocated with the snowband over Lake Ontario and along the axis of the Saint

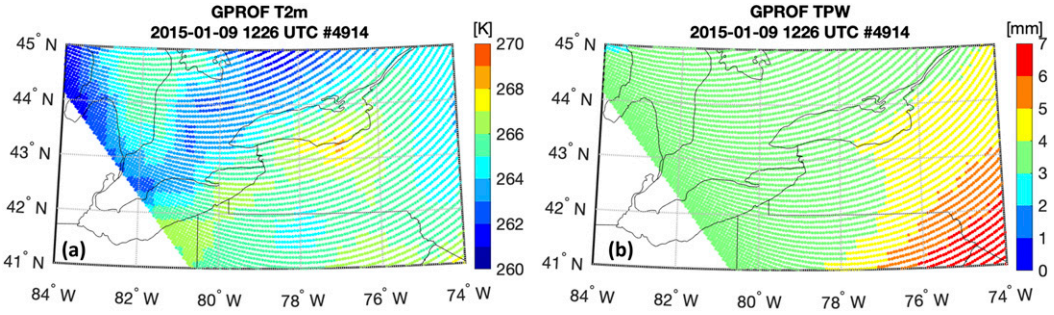

FIG. 5. As in Fig. 1, but for 1226 UTC 9 Jan 2015.

Lawrence River. Both 89- and 166-GHz TB trends over Lake Ontario followed similar patterns as the previous case study, with warmer emission signals against the cold lake background evolving into scattering signals. Reduced ΔTB_{89} and ΔTB_{166} magnitudes over Lake Ontario surfaces also coincided with lake-effect clouds and snowbands. Interestingly, 166-GHz and $\Delta TB_{183.31}$ scattering signatures accompanying the Lake Ontario snowband appeared slightly stronger than the Lake Erie band despite obviously weaker NEXRAD characteristics (Fig. 6). This disparity might reflect NEXRAD range-dependent artifacts related to the Lake Erie band's proximity to the KBUF radar compared to the Lake Ontario band to KTYX radar site distance. Furthermore, the KTYX radar is physically located on the elevated Tug Hill Plateau ~350 m higher above sea level than the KBUF site.

2) GPROF PERFORMANCE

As opposed to the first case study, GPROF classifies the surface as coastline on both southern sides of the lake shores (Fig. 8d), even though inland surfaces near the lake are more likely snow-covered since the GPM-CO orbit occurs on the second day of a three-day extreme snowfall event. As a matter of fact, the National Weather Service Snow Analysis (NSA; NWS 2019) indicates that surfaces on the south and east sides of the lakes were covered by 10–25 cm of snow on 8 and 9 January 2015. The NSA also estimated snowpack temperatures between −5° and −20°C and no melting. We can then speculate that the AutoSnow product did not detect surface snowpack (note that AutoSnow does not provide any output under cloudy conditions). Therefore, GPROF uses the DPR a priori database for pixels classified as coastline or land for this case study, including most of the southern shore of the lakes where NEXRAD observes intense snowfall. Recall that GPROF used the GV-MRMS a priori database for snow-covered surfaces correctly defined in the previous case study (Fig. 4d).

The pixel-by-pixel comparison between operational GPROF and GV-MRMS (not shown), in this case does not show any correlation and while GV-MRMS shows rates up to 1 mm h^{-1} most GPROF precipitation rates lie within 0.03 and 0.11 mm h^{-1}.

The PRT method is tested (PRT = 0.11 mm h^{-1}) but does not produce a precipitation pattern similar to the GV-MRMS for this case (Fig. 8c). Table 1 shows the statistical GPROF-GV-MRMS scores obtained after applying the PRT filter. The detection scores are very low for the operational GPROF (HSS = −0.01) and slightly better for PRT (HSS = 0.11), but overall reflect poor PMW algorithm performance. FAR is also consistently elevated, with values of 0.80 and 0.54 for the operational GPROF and PRT, respectively. Correlation values improve from 0.43 (operational GPROF) to 0.51 when the PRT is applied.

It is worth noting DPR data are available and included in the DPR a priori database for this case. The DPR covers the inner part of GMI swath, providing precipitation estimates only over Lake Ontario (Fig. 8e). The DPR shows a snowband similar to the GV-MRMS structure with moderate to intense rates. The storm-top height (Fig. 8f) confirms that DPR can detect LES events with vertical extension between 1 and 4 km (at least for the central pixels of the swath). Despite the exact GV-MRMS and DPR surface precipitation rates being included in the a

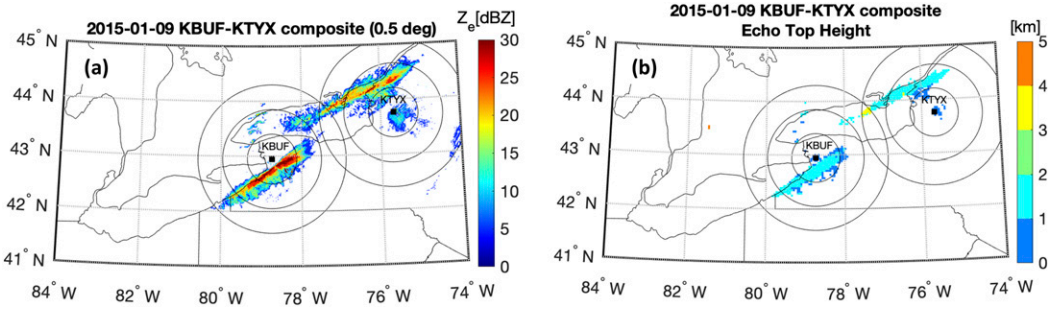

FIG. 6. As in Fig. 2, but for 1228 and 1224 UTC 9 Jan 2015.

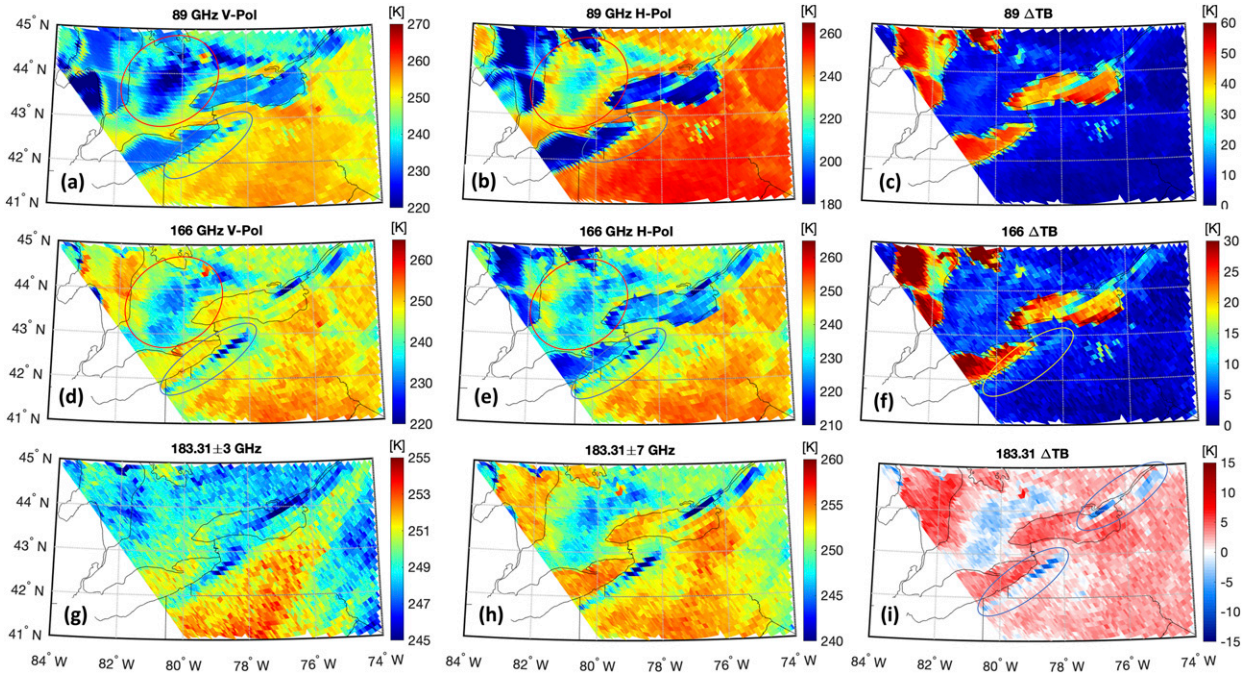

FIG. 7. As in Fig. 3, but for the GPM-CO overpass near 1226 UTC 9 Jan 2015 (GPM-CO orbit 4914). Circles are added here to highlight some of the important features described in the text.

priori databases for this event, GPROF assigns low Bayesian weights to those profiles, making the weighted average more centered on similar profiles that are most likely not precipitating. The result is a very smoothed precipitation rate and pattern that does not detect snowfall when strong filters are applied. As already mentioned, the case studies considered in this work have been purposefully chosen within the period included in the a priori databases to show that even if GMI TBs clearly indicate multifrequency signatures and DPR and GV-MRMS provide surface snowfall rate estimates in their respective a priori databases, GPROF cannot convert that information into a physically consistent or realistic retrieval. Because of the a priori database searching method within a specific surface, T2m and TPW subset, misclassifying the surface type or the modeled environmental conditions heavily affects the algorithm output. These potential issues and possible solutions for users and algorithm developers are investigated further in section 4.

4. Analysis of GPROF retrieval components

In the following subsections, we will analyze the most important algorithm components and their potential role in the performance inconsistencies outlined in section 3. Algorithm improvement pathways are also offered.

a. A priori database representativeness

Since GPROF retrievals fundamentally rely on a priori GMI radiance–surface-precipitation-rate information, the representativeness of the a priori databases for intense LES events is investigated. Considering a 0.1 mm h^{-1} threshold for precipitation (in agreement with the GV-MRMS threshold used for this study and very close to the PRT threshold for the case studies analyzed), Fig. 9 shows the 2D joint distribution of precipitating elements in the a priori databases. Considering the two cases presented in section 3 and the radiosonde data of several intense LES events, we consider TPW = 5 mm and T2m = 273 K as appropriate thresholds for LES event conditions over the analyzed region. The thresholds are chosen based on 61 intense LES events reported by the Buffalo NWS office (NWS 2020) over the past 6 winter seasons (2014–20), where 80% of the events showed TPW ≤ 5 mm and the other 20% between 5 and 7 mm. The temperature threshold of 273 K represents the upper limit defined by Kunkel et al. (2002) for "severe" LES storms (the defined range is 263 to 273 K for storms with 24 h accumulation > 35 cm). According to Kunkel et al. (2002), "heavy" events (24 h snow accumulation between 20 and 35 cm) always occur between 258 and 263 K. The number of coastline and snow-covered precipitating elements in the global a priori database within the TPW ≤ 5 mm and T2m ≤ 273 K subsets (bins in the bottom left corner of Fig. 9 plots, red lines plotted as reference) is quite low, with just 1.3% (0.1%) of all precipitating elements (all elements) in the coastline database subset (Fig. 9a) and with values between 7% and 11% (0.5% and 0.7%) of all precipitating elements (all elements) in the snow-covered surface database subsets (Figs. 9b–e). Relative to the GV-MRMS database, the lower percentages of the a priori database for coastline, which is based on DPR data, are a clear indication that LES (or in general precipitation events associated to the same environmental conditions as LES), in the coastline database is underrepresented, especially considering that snow occurrences at coastline and

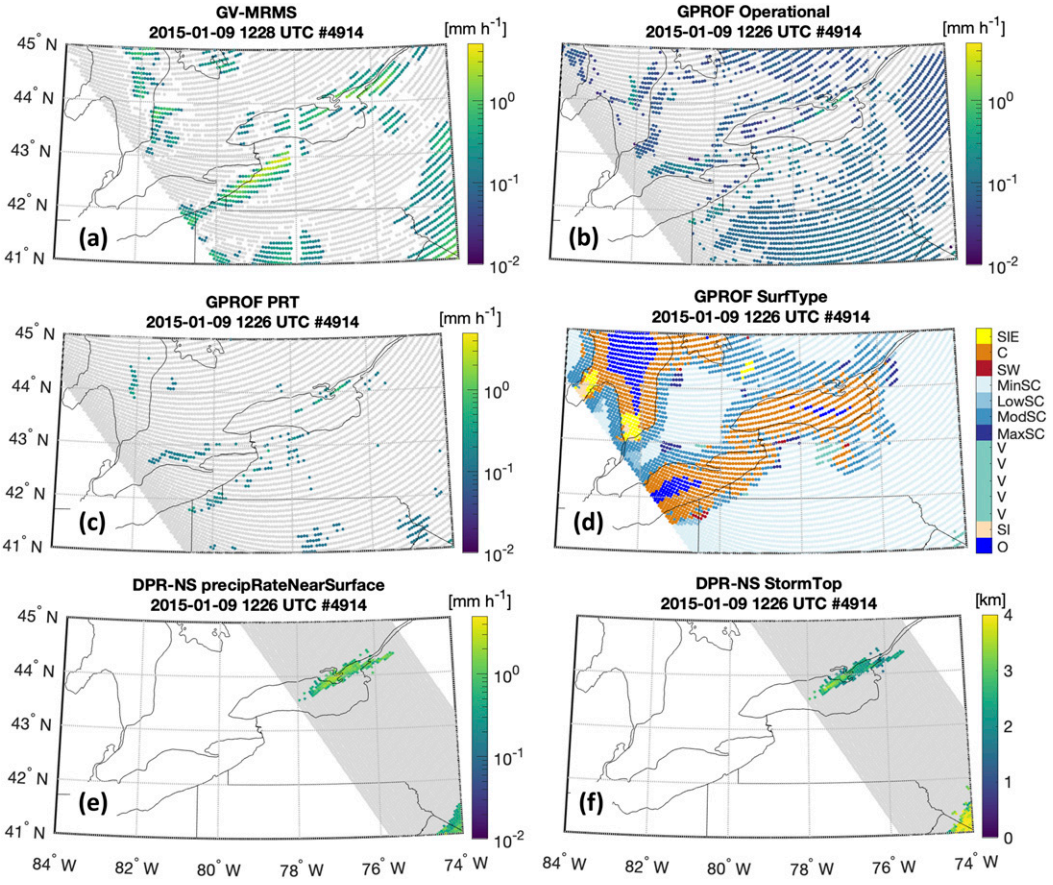

FIG. 8. (a) MRMS-GV snowfall rate over Lakes Erie and Ontario at 1226 UTC 9 Jan 2015 (orbit 4914), (b) GPROF precipitation rate (using the SurfPrecip parameter from the operational product), (c) GPROF PRT precipitation rate ($\geq$0.11 mm h^{-1}), (d) surface classification as from the GPROF SurfType parameter (as in Fig. 4), (e) DPR precipitation rate (using the Normal Scan PrecipRateNearSurface parameter), and (f) DPR storm-top height.

nearby snow cover should be similar. While the precipitation conditions over snow-covered surfaces are most likely solid (of course not always), the coastal subset includes all the global coastal elements, so it includes tropical precipitation events as well as midlatitude or high-latitude liquid precipitation. Moreover, the DPR a priori database is built only with one winter season, which lowers even further the probability of finding LES elements within the database. On the other hand, the GV-MRMS-based database, which is only used for snow-covered surfaces, has a reasonable representation of LES (0.5%–0.7%), even though it might be still well below the actual occurrence considering that the global shallow convection snowfall occurrence is 36% (Kulie et al. 2016) and that LES accounts for almost 80% occurrence and 50% contribution to annual snowfall accumulation in the upper Great Lakes (Pettersen et al. 2020). Among the several factors contributing to the underrepresentation of LES in the GV-MRMS a priori database we can mention the quality filters applied to the GV-MRMS precipitation product (only high-quality is considered in the GPROF a priori database). Additionally, the fixed Z–S relationship (not necessarily suited for LES snowfall retrieval), or the missed shallow LES bands distant from the radar, are responsible for underestimation or underdetection of LES events. Finally, limiting the a priori database to two winter seasons only, does not guarantee a statistically meaningful number of LES entries. The percentage of LES events compared with deeper and more extended synoptic events is still too low for a Bayesian algorithm. Therefore, low T2m and TPW values are not common in the precipitation-rate distributions and the a priori databases do not contain a large amount of elements under these conditions.

Precipitation-rate probability density functions (PDFs) of each a priori database subset illustrate the low probability of higher precipitation-rate events within the database. Precipitation-rate PDFs of all precipitation (symbols) and of precipitating elements with T2m $\leq$ 273 K and TPW $\leq$ 5 mm (symbols with solid lines) are shown in Fig. 10. The coastline (asterisks) and maximum snow-cover (diamonds) data points associated with the most probable LES conditions (symbols with solid lines) contain only 120 and 126 elements with precipitation rates over 1 mm h^{-1}, respectively. Only

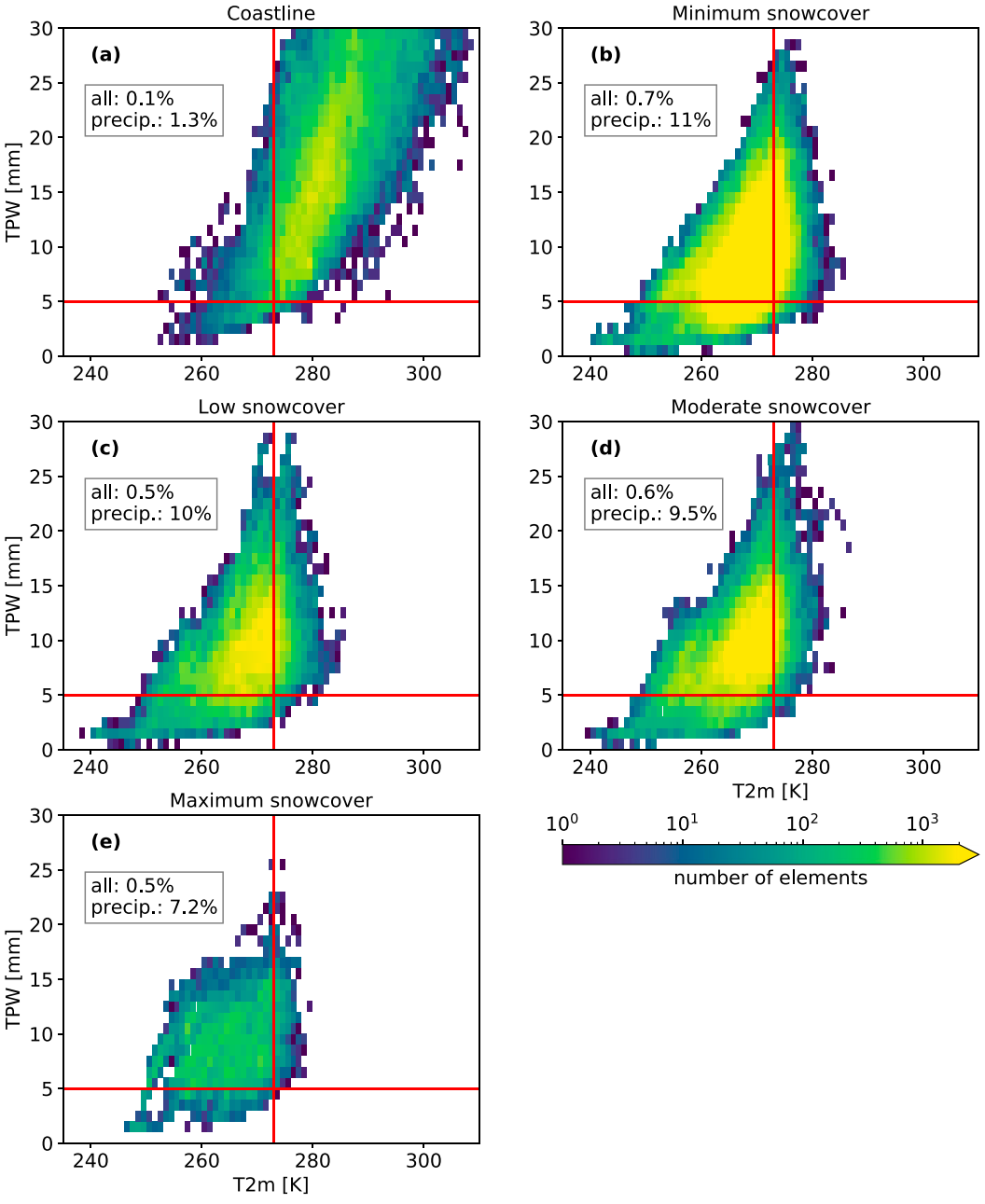

FIG. 9. The 2D distributions of GPROF a priori database elements (surface precipitation elements with PR $\geq$ 0.1 mm h^{-1}); red lines for T2m = 273 K and TPW = 5 mm are plotted as reference. Percentage of surface precipitation elements within the TPW $\leq$ 5 mm and T2m $\leq$ 273 K subsets for each surface database subsets calculated over the total number of elements (all), and over the number of precipitating elements (precip) are also shown for each distribution. (a) DPR a priori database is used for coastline, and GV-MRMS a priori database is used for (b) minimum snow cover, (c) low snow cover, (d) moderate snow cover, and (e) maximum snow cover.

0.3% among all precipitating elements contained in each snow-covered a priori database subset contains rates above 1 mm h^{-1}. The percentage decreases to 0.03% for the coastal subset. This analysis suggests that on a global basis, finding an optimal database match for intense LES events is very difficult, especially for coastline surfaces that represent the most common surface for the two case studies analyzed. Incorrectly characterizing the background surface in the 4914 case represents a likely reason for poor algorithm performance. A pixel-by-pixel a priori database investigation indicates that there are many low rates (<0.01 mm h^{-1}) precipitating elements with similar TBs values that are considered by the Bayesian algorithm with nonnegligible Bayesian weights. This causes the Bayesian algorithm to

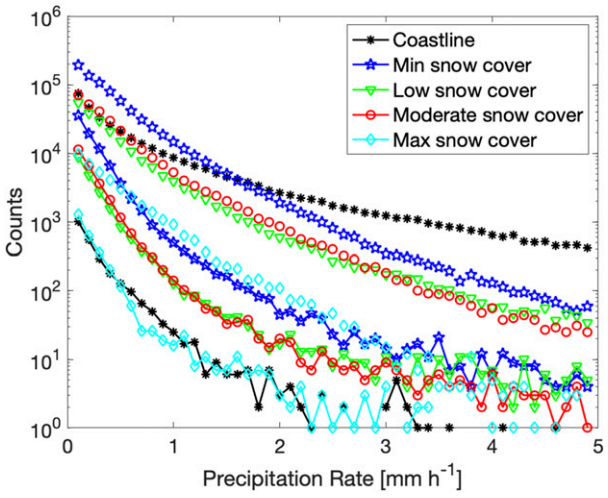

FIG. 10. Probability density functions of precipitation rates associated with precipitating elements in the a priori databases. Symbols represent the distribution of all precipitating events (PR $\geq$ 0.1 mm h^{-1}); symbols with solid lines represent precipitating events with T2m $\leq$ 273 K and TPW $\leq$ 5 mm. Colors represent the different surface types.

smooth the output rates or miss them completely. A more detailed analysis on the a priori database TBs distribution is provided in the following section 4b. Populating the a priori databases with additional LES cases (e.g., adding more years of observations) or adding constraints to identify such cases and create a separate ''shallow convective'' database would improve algorithm performance.

b. *TB-snowfall rate outliers in the a priori database*

After analyzing the representativeness of the a priori databases considering the occurrence of snowfall elements (with snowfall rates $\geq$ 0.1 mm h^{-1}) under LES environmental conditions, we now verify to what extent these same elements are represented in the multichannel TB space, in particular at higher frequency. The GPROF search is based on a Bayesian scheme in the TB space, so if the algorithm cannot find TB elements relatively similar to the measured TBs the algorithm will continue to expand the search bins until some minimum number is included, it will include profiles from different bins, but the retrieval will be less accurate. The goal here is to verify how the TBs measured in the higher-frequency channels for the LES case studies, and for extreme environmental conditions, compare with the TBs of the a priori surface category subset that is assigned by GPROF in such conditions.

The two case studies (GPM-CO orbits 4140 and 4914) presented in section 3 are analyzed further to verify if these situations can be defined as outliers from a TB-surface snowfall rate perspective that make it more difficult, if not impossible, for the algorithm to find a correct match with a priori database entries. Figure 11 illustrates, for coastline and minimum snow-cover surface types, boxplots of global TBs (blue thicker boxes) considering only the precipitating elements (PR $\geq$ 0.1 mm h^{-1}, left column) and all the elements (right column) of the a priori subsets of TPW and T2m values for the cases analyzed (T2m = 269–271 K and TPW = 4 mm for orbit 4140 and T2m = 262–266 K and TPW = 3–4 mm for orbit 4914). TB boxplots for the selected cases over the Lake Erie and Ontario region are also shown (red thinner boxes).

Most of the intense snowbands from the case studies occur over coastline (Figs. 4d and 8d) with 50.6% (33.2%) of precipitating pixels for orbit 4140 (4914) and smaller portions over minimum snow cover (25.3% and 41.3%, respectively) and moderate snow cover (21.7% and 19.2%). The coastline boxplots (Figs. 11a–d) clearly explain why GPROF performs better for the 4140 case. The 4914 a priori database and the single orbit 89-GHz TB distributions are very different. The median of the 166-GHz TB distribution also falls out of the 25th to 75th percentile range of the a priori database distributions (Fig. 11c). The only channel that shows similar database and orbit TB distributions is 183.31 $\pm$ 3 GHz, but this channel alone cannot resolve the signal and translate it into a realistic retrieval despite its sensitivity to snowfall-scattering signatures. Without examples of these particular TB distributions, the a priori database cannot correctly detect and retrieve the precipitation rate for this event. Conversely, even if the TB distributions for the 4140 case do not perfectly fit within the 25th–75th percentile range of the a priori database distributions, most of the channels substantially overlap and provide at least some useful retrieval information.

The minimum snow-covered surface category TB distributions portray a very different situation than the coastline category. The 4140 orbit TB distributions appear disconnected and suggest poor GPROF results, while the 4914 distributions are relatively centered. The results, however, show a completely opposite interpretation. Comparing the TB distributions of precipitating elements of the a priori database (Figs. 11e,g; blue thicker boxes) with the distributions of all (precipitating and nonprecipitating) a priori database elements (Figs. 11f,h; blue thicker boxes), the total distributions extend toward colder temperatures (instead of warmer as expected for nonprecipitating elements). Low TPW values and clear-sky conditions allow both 89- and 166-GHz channels to probe closer to the surface and are contaminated by the cold snow-covered surface signature. This particular behavior matches colder snowband TB scattering signatures with nonsnowing cold TB a priori database elements. Moreover, the TB distributions of precipitating elements extracted from the orbit 4140 visibly differ from TB distributions comprised of precipitating and nonprecipitating elements (Figs. 11e,f; red thinner boxes), thus providing some useful information for the retrieval. However, the 4914 orbit TB distributions extend their ranges, but do not substantially change. The very similar distributions between precipitating and all elements at low T2m and TPW ranges do not help the algorithm assign higher Bayesian weights to any of the elements, with consequent detrimental quantification and detection ramifications.

This second analysis provides new and important information about the a priori database. From section 4a, the distribution of precipitating elements based on low T2m and TPW are not statistically represented for coastline and snow-covered surfaces (Fig. 9). Additionally, intense snow rates events are

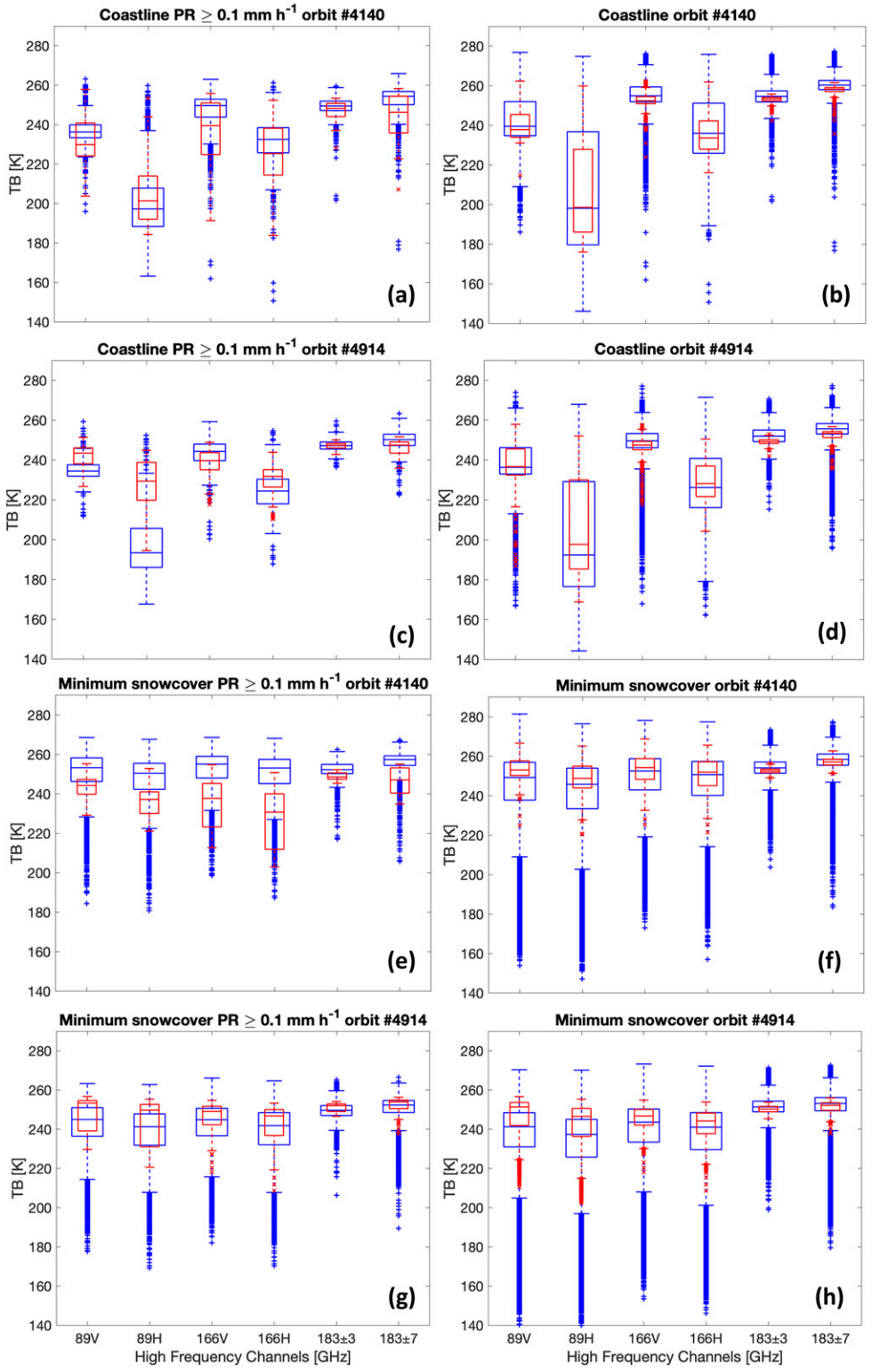

FIG. 11. (left) Boxplots of high-frequency channel TBs for precipitating elements (PR ≥ 0.1 mm h^{-1}) of the a priori database associated with T2m and TPW in the case studies range (blue thicker boxes) and TBs for the precipitating pixels of the case studies (red thinner boxes). (right) All a priori database elements (precipitating and nonprecipitating). GPM-CO orbits 4140 and 4914 are shown for (a)–(d) coastline and (e)–(h) minimum snow cover.

TABLE 2. Statistical scores for the two case studies forcing GPROF to use the GV-MRMS-only a priori database. The results are obtained applying the PRT, and the thresholds considered case by case are also shown.

	Threshold (mm h^{-1})	HSS	FAR	CSI	r
4140	0.13	0.35	0.30	0.26	0.67
4914	0.1	0.29	0.43	0.24	0.22

not included in the a priori database (Fig. 10). The TB distributions analyzed in this section confirm that coastline and minimum snow surface TB database entries are underrepresented for extreme LES events. Low, moderate, and maximum snow-covered surfaces were not included in this latter analysis because of the very low pixel counts associated with LES bands over the orbital regions considered.

c. *Surface classification*

GPROF surface classification methodologies were also tested, based on the premise that GPROF searches the GV-MRMS a priori database if the emissivity-based surface classification and/or AutoSnow product suggest a snow-covered surface. Recall that the GV-MRMS snowfall rate a priori database was developed to extend the DPR snowfall rate a priori database and better represent the lower end of the snowfall rate spectrum. The operational a priori database selection is based on the monthly emissivity-based surface classification or is updated using the AutoSnow product on the day before the specific orbit date. AutoSnow is not available under cloudy conditions. Considering that LES events can span multiple days, all surfaces are now assumed to be snow covered for testing purposes. Therefore, GPROF is adapted to use the GV-MRMS a priori database exclusively for all pixels in the following analysis.

The ensuing results are encouraging from both detection and quantification viewpoints. Table 2 presents statistical scores obtained by applying the PRT with the minimum snowfall rate threshold defined case by case from the highest HSS score. Compared to Table 1, the FAR for orbit 4140 (4914) decreases from 0.57 (0.54) to 0.30 (0.43). The CSI and HSS also increase relative to the operational and PRT results. Figure 12 displays updated QPE results of the two case studies. For orbit 4140, the Lake Erie snowband (originally classified as coastline and now forced to be snow covered) is correctly detected and the core of the band shows comparable snow rates (Fig. 12a compared to Fig. 4a). The GPROF PRT–GV-MRMS correlation increases from 0.61 (Table 1) to 0.67 (Table 2), and precipitation rates are higher when forcing the GV-MRMS-only a priori database (Fig. 4c compared to Fig. 12a). On the other hand, the snowband over Lake Ontario and lower snow rates over land in the eastern part of the domain (42°–43°N 74°–76°W) are almost completely missed. Results for orbit 4914 are also improved (Fig. 12b). The snowband pattern over the coast of Lake Erie, completely missed in Fig. 8c, is now detected, albeit with significant QPE issues. Forcing GPROF to use the GV-MRMS a priori database exclusively also improves the Lake Ontario snowband detection that was only partially noted in Fig. 8c. It is worth noting that the major improvements are achieved over what was originally defined as coastline surface by the algorithm, highlighting the fact that with a different surface classification the retrieval can be improved. Figure 12 clearly shows that there are still detection issues over land and a general underestimation of snowfall rates, but the test example identifies surface classification as a major algorithm component worth improving.

5. Conclusions

Intense LES detection and QPE by the GPM-CO PMW sensor is addressed in this study. Two case studies were analyzed over the Lower Great Lakes region. NEXRAD observations in this region effectively observed these events and serve as GPM-CO evaluation datasets. It is particularly important to investigate the GMI high-frequency TB response to this globally ubiquitous type of shallow convective snow and optimize the GPM GPROF algorithm for these extreme winter precipitation events.

Both case studies (orbit 4140 on 20 November 2014 and orbit 4914 on 9 January 2015) show GMI distinct TB scattering signatures (e.g., 166- and 183.31-GHz TB depressions) associated with intense LES bands that match NEXRAD reflectivity patterns. These scattering signatures were also evident over varying surface types (e.g., open water vs snow-covered land) and highlight the importance of high-frequency GMI channels for snowfall detection purposes. Despite clear observational

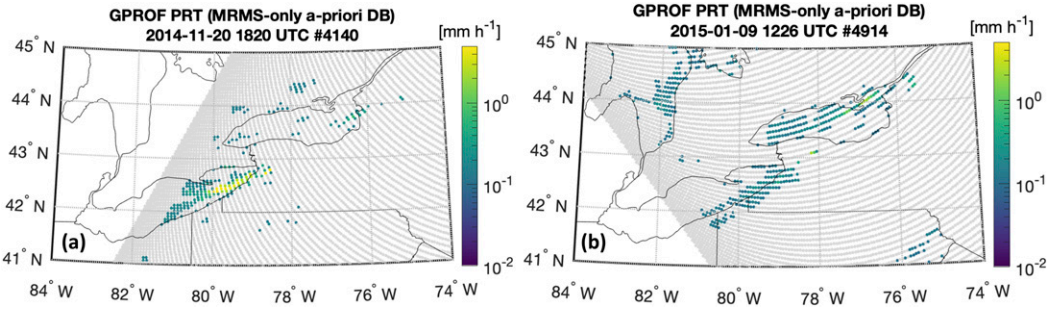

FIG. 12. Maps of GPROF estimates made forcing the GV-MRMS-only a priori database for (a) orbit 4140 and for (b) orbit 4914.

TB signals and extreme surface precipitation rates, the GMI GPROF algorithm inconsistently inverts the TB signal into realistic precipitation rates. Both detection and QPE performance metrics are low when compared to ground-based GV-MRMS radar network products.

A precipitation-rate threshold (PRT) was adopted to effectively filter low-quality GPROF retrievals and improve comparisons with GV-MRMS. The threshold was obtained case by case by using a minimum precipitation rate that optimized HSS values. Quantitatively speaking, GPROF generally underestimates precipitation when compared to GV-MRMS, but better correlation results are obtained with GPROF PRT. Product users should consider adopting this precipitation threshold methodology when evaluating GPROF retrievals for individual snowfall events.

GPROF relies on a priori TB–precipitation-rate databases to generate QPE retrievals for each GMI observation, with different databases applied to underlying surface types for snowfall events. The DPR (land/coast surfaces) and the GV-MRMS (snow-covered surfaces) GPROF a priori databases are found to be underpopulated with observations for these intense LES events that occur in cold, dry environments over complex surface types, thus making it difficult for GPROF to generate plausible retrievals. Moreover, even if the analyzed orbital observations are included in the a priori databases, the presence of nonprecipitating elements with similar TB characteristics significantly smooth the retrievals and cause retrieval underestimation issues. A final a priori database sensitivity test was attempted by forcing GPROF to use the GV-MRMS-only a priori database over all surface types for both case studies. These tests demonstrate GPROF detection and QPE performance improvements and suggest that better characterizing the surface type and/or applying the GV-MRMS-only database on a wider basis will improve GPROF snowfall retrievals.

In summary, this study offers the following research activities to improve GPROF QPE performance for extreme LES events:

- Shallow, convective snowfall events that form in low TPW and cold environments are underrepresented in GPROF a priori databases, especially for coastline and snow-covered surfaces. Further testing should be undertaken with GPROF a priori databases that are populated with more lake-effect/shallow convective snow profiles, mainly over coast and snow-covered surfaces. Additional years of GPM and/or GV-MRMS observations should also be included in the a priori database. Furthermore, an expanded role of the GV-MRMS database should be explored to quantify potential GPROF performance improvements. Matched *CloudSat*–GPM observations also represent a valuable source of shallow convective snow observations to be included in an expanded a priori database.
- The surface classification, based on monthly emissivity climatologies and the NOAA AutoSnow product, does not correctly classify some snow-covered surfaces (mainly over coastlines under cloudy conditions) and points the algorithm to the wrong (snow cover free) a priori database. Snow cover has distinct and extremely variable (in space and time) radiative properties that, especially in extremely dry conditions, affect the brightness temperatures at all frequencies. Therefore, in such conditions the TB dependence on the a priori database background surface categorization is extremely critical. It is fundamental to be able to characterize the surface background and to correctly convey this information in the retrieval process. An updated surface emissivity database developed by Munchak et al. (2020) for surface characterization based on five years of GPM observations should be considered to improve intense LES retrievals. The exploitation of GMI low-frequency channels at the time of the overpass could offer extremely useful insights on the status of the frozen surface background. A number of studies already investigated the information content in the TBs to separate the surface signal from precipitation signal on an orbit basis (e.g., Rysman et al. 2018; Ebtehaj et al. 2020; Turk et al. 2018). The use of a dynamic frozen surface characterization approach could benefit GPROF snowfall detection and retrieval.
- Similar to convective/stratiform rainfall partitioning schemes, snowfall type flags could be introduced to force GPROF to adopt specific settings (e.g., a specific a priori database with only shallow convective or stratiform snowfall events, precipitation thresholds). Preliminary studies used the combined *CloudSat*–GPM dataset (Turk 2016) and a machine learning technique to train GMI reflectivities to classify the snowfall mode, based on the *CloudSat* shallow convective retrieval algorithm (Kulie et al. 2016). Results have shown high overall accuracy in GMI classifying snowfall type (convective vs stratiform), suggesting future avenues to further improve the GPROF algorithm.

The GMI sensor possesses tremendous promise for detecting intense convective snow events based on the analysis presented in this study. The GPROF algorithm, however, currently struggles to consistently translate distinctive GMI TB signals into realistic precipitation rates and highlights the inherent complexities associated with PMW retrievals of LES, even for extreme snowfall-producing events. TB analysis with full GPM constellation is planned in order to understand how different spatial resolution and scanning capabilities could impact the detection and quantification of LES narrow and localized snowbands. This study offers numerous pathways forward to improve algorithm performance for shallow convective snow so the unique observational capabilities of the GMI and affiliated GPM constellation satellites can be better capitalized for high-latitude snowfall research.

Acknowledgments. Doctor Lisa Milani has been funded by the NASA GPM Mission. This work was partially funded by NASA Grants 80NSSC19K0681 and NNX16AL23G (Dr. Pierre E. Kirstetter), NASA Grants 80NSSC17K0058, 80NSSC17K0291, and NNX16AE21G (Dr. Mark Kulie), and NOAA Grant NA19NES4320002 (Dr. Veljko Petković). This work was also supported by the EUMETSAT H SAF (CDOP-3), and by the RainCast study (ESA Contract 4000125959/18/NL/NA). The PMM Research Program and EUMETSAT are acknowledged for supporting H SAF and GPM scientific collaboration

through the approval of the no-cost H SAF-GPM proposal "H SAF and GPM: precipitation algorithm development and validation activity." Dr. Jean-François Rysman was supported by the Direction Générale de l'Armement (PRECIPCLOUD-SAT Project) and by the CNES. The generous support by the National Science Foundation (NSF) under conference Grant EAR-1928724 and by NASA under conference Grant 80NSSC19K0726 for the organization of the 12th International Precipitation Conference (IPC12) is gratefully acknowledged. The authors sincerely thank the three anonymous reviewers for their very valuable and constructive comments and suggestions. The views, opinions, and findings contained in this report are those of the authors and should not be construed as an official National Oceanic and Atmospheric Administration or U.S. government position, policy, or decision.

Data availability statement. For this study, the 1C-R-GMI product (TBs) and the 2A-GPROFGMI (precipitation rates and environmental information) have been used. These datasets are freely available through the NASA Precipitation Processing System (PPS) data archive (https://storm.pps.eosdis.nasa.gov/storm/). The MRMS dataset is available online from the NASA Global Hydrology Center DAAC, Huntsville, Alabama (https://doi.org/10.5067/GPMGV/MRMS/DATA101) as cited by Kirstetter et al. (2018). Snow depth and snowpack temperatures are available from the National Weather Service Snow Analysis (https://www.nohrsc.noaa.gov/nsa/), and the Lake Effect Snow Event Archive is available online (https://www.weather.gov/buf/lesEventArchive?season=2017-2018&event=A). Radiosonde data from the National Weather Service Weather Forecast Offices are available from the University of Wyoming College of Engineering (http://weather.uwyo.edu/upperair/sounding.html), and the surface temperature analyses are available from the NOAA Great Lakes Environmental Research Laboratory (https://coastwatch.glerl.noaa.gov/glsea/glsea.html).

REFERENCES

Adhikari, A., C. Liu, and M. S. Kulie, 2018: Global distribution of snow precipitation features and their properties from 3 years of GPM observations. *J. Climate*, **31**, 3731–3754, https://doi.org/10.1175/JCLI-D-17-0012.1.

Adler, R. F., J.-J. Wang, G. Gu, and G. J. Huffman, 2009: A ten-year tropical rainfall climatology based on a composite of TRMM products. *J. Meteor. Soc. Japan*, **87A**, 281–293, https://doi.org/10.2151/jmsj.87A.281.

Aires, F., C. Prigent, F. Bernardo, C. Jimenez, R. Saunders, and P. Brunel, 2011: A Tool to Estimate Land-Surface Emissivities at Microwave frequencies (TELSEM) for use in numerical weather prediction. *Quart. J. Roy. Meteor. Soc.*, **137**, 690–699, https://doi.org/10.1002/qj.803.

Benjamin, S. G., and Coauthors, 2004: An hourly assimilation–forecast cycle: The RUC. *Mon. Wea. Rev.*, **132**, 495–518, https://doi.org/10.1175/1520-0493(2004)132<0495:AHACTR>2.0.CO;2.

Casella, D., G. Panegrossi, P. Sano, A. C. Marra, S. Dietrich, B. T. Johnson, and M. S. Kulie, 2017: Evaluation of the GPM-DPR snowfall detection capability: Comparison with CloudSat-CPR. *Atmos. Res.*, **197**, 64–75, https://doi.org/10.1016/j.atmosres.2017.06.018.

Dee, D. P., and Coauthors, 2011: The ERA-Interim reanalysis: Configuration and performance of the data assimilation system. *Quart. J. Roy. Meteor. Soc.*, **137**, 553–597, https://doi.org/10.1002/qj.828.

Draper, D. W., D. A. Newell, F. J. Wentz, S. Krimchansky, and G. M. Skofronick-Jackson, 2015: The Global Precipitation Measurement (GPM) Microwave Imager (GMI): Instrument overview and early on-orbit performance. *IEEE J. Sel. Top. Appl. Earth Obs. Remote Sens.*, **8**, 3452–3462, https://doi.org/10.1109/JSTARS.2015.2403303.

Ebtehaj, A. M., and C. D. Kummerow, 2017: Microwave retrievals of terrestrial precipitation over snow-covered surfaces: A lesson from the GPM satellite. *Geophys. Res. Lett.*, **44**, 6154–6162, https://doi.org/10.1002/2017GL073451.

——, ——, and F. J. Turk, 2020: Metric learning for approximation of microwave channel error covariance: Application for satellite retrieval of drizzle and light snowfall. *IEEE Trans. Geosci. Remote Sens.*, **58**, 903–912, https://doi.org/10.1109/TGRS.2019.2941682.

Edel, L., J.-F. Rysman, C. Claud, C. Palerme, and C. Genthon, 2019: Potential of passive microwave around 183 GHz for snowfall detection in the Arctic. *Remote Sens.*, **11**, 2200, https://doi.org/10.3390/rs11192200.

Gong, J., and D. L. Wu, 2017: Microphysical properties of frozen particles inferred from Global Precipitation Measurement (GPM) Microwave Imager (GMI) polarimetric measurements. *Atmos. Chem. Phys.*, **17**, 2741–2757, https://doi.org/10.5194/acp-17-2741-2017.

Grecu, M., and Coauthors, 2016: The GPM combined algorithm. *J. Atmos. Oceanic Technol.*, **33**, 2225–2245, https://doi.org/10.1175/JTECH-D-16-0019.1.

Hamada, A., and Y. N. Takayabu, 2016: Improvements in detection of light precipitation with the Global Precipitation Measurement Dual-Frequency Precipitation Radar (GPM DPR). *J. Atmos. Oceanic Technol.*, **33**, 653–667, https://doi.org/10.1175/JTECH-D-15-0097.1.

Hou, A. Y., and Coauthors, 2014: The Global Precipitation Measurement Mission. *Bull. Amer. Meteor. Soc.*, **95**, 701–722, https://doi.org/10.1175/BAMS-D-13-00164.1.

Iguchi, T., 2020: Dual-frequency Precipitation Radar (DPR) on the Global Precipitation Measurement (GPM) Mission's Core Observatory. *Satellite Precipitation Measurement*, V. Levizzani et al., Eds., Springer, 183–192.

JMA, 2000: New numerical analysis and forecast system. Japan Meteorological Agency Annual Rep. 33, 143 pp.

Kirschbaum, D. B., and Coauthors, 2017: NASA'S remotely sensed precipitation: A reservoir for applications users. *Bull. Amer. Meteor. Soc.*, **98**, 1169–1184, https://doi.org/10.1175/BAMS-D-15-00296.1.

Kirstetter, P.-E., and Coauthors, 2012: Toward a framework for systematic error modeling of spaceborne precipitation radar with NOAA/NSSL ground radar–based national mosaic QPE. *J. Hydrometeor.*, **13**, 1285–1300, https://doi.org/10.1175/JHM-D-11-0139.1.

——, Y. Hong, J. J. Gourley, Q. Cao, M. Schwaller, and W. Petersen, 2014: Research framework to bridge from the Global Precipitation Measurement Mission Core satellite to the constellation sensors using ground-radar-based National Mosaic QPE. *Remote Sensing of the Terrestrial Water Cycle*, V. Lakshmi et al., Eds., John Wiley and Sons, 61–79, https://doi.org/10.1002/9781118872086.ch4.

——, J. J. Gourley, Y. Hong, J. Zhang, S. Moazamigoodarzi, C. Langston, and A. Arthur, 2015: Probabilistic precipitation

rate estimates with ground-based radar networks. *Water Resour. Res.*, **51**, 1422–1442, https://doi.org/10.1002/2014WR015672.

——, W. A. Petersen, and J. J. Gourley, 2018: GPM Ground Validation Multi-Radar/Multi-Sensor (MRMS) Precipitation Reanalysis for Satellite Validation Product. NASA Global Hydrology Resource Center DAAC, accessed 25 November 2020, https://doi.org/10.5067/GPMGV/MRMS/DATA101.

Kneifel, S., J. Leinonen, J. Tyynela, D. Ori, and A. Battaglia, 2020: Scattering of Hydrometeors. *Satellite Precipitation Measurement*, V. Levizzani et al., Eds., Springer, 249–276.

Kongoli, C., P. Pellegrino, R. R. Ferraro, N. C. Grody, and H. Meng, 2003: A new snowfall detection algorithm over land using measurements from the Advanced Microwave Sounding Unit (AMSU). *Geophys. Res. Lett.*, **30**, 1756, https://doi.org/10.1029/2003GL017177.

——, H. Meng, J. Dong, and R. Ferraro, 2015: A snowfall detection algorithm over land utilizing high-frequency passive microwave measurements—Application to ATMS. *J. Geophys. Res. Atmos.*, **120**, 1918–1932, https://doi.org/10.1002/2014JD022427.

Kozu, T., and Coauthors, 2001: Development of precipitation radar onboard the Tropical Rainfall Measuring Mission (TRMM) satellite. *IEEE Trans. Geosci. Remote Sens.*, **39**, 102–116, https://doi.org/10.1109/36.898669.

Kubota, T., T. Iguchi, M. Kojima, L. Liao, T. Masaki, H. Hanado, R. Meneghini, and R. Oki, 2016: A statistical method for reducing sidelobe clutter for the Ku-band precipitation radar on board the GPM *Core Observatory*. *J. Atmos. Oceanic Technol.*, **33**, 1413–1428, https://doi.org/10.1175/JTECH-D-15-0202.1.

Kulie, M. S., and R. Bennartz, 2009: Utilizing spaceborne radars to retrieve dry snowfall. *J. Appl. Meteor. Climatol.*, **48**, 2564–2580, https://doi.org/10.1175/2009JAMC2193.1.

——, and L. Milani, 2018: Seasonal variability of shallow cumuliform snowfall: A CloudSat perspective. *Quart. J. Roy. Meteor. Soc.*, **144**, 329–343, https://doi.org/10.1002/qj.3222.

——, ——, N. B. Wood, S. A. Tushaus, R. Bennartz, and T. S. L'Ecuyer, 2016: A shallow cumuliform snowfall census using spaceborne radar. *J. Hydrometeor.*, **17**, 1261–1279, https://doi.org/10.1175/JHM-D-15-0123.1.

——, ——, ——, and T. S. L'Ecuyer, 2020: Global snowfall detection and measurement. *Satellite Precipitation Measurement*, 1st ed. V. Levizzani et al., Eds., Springer, 699–716.

Kummerow, C., W. S. Olson, and L. Giglio, 1996: A simplified scheme for obtaining precipitation and vertical hydrometeor profiles from passive microwave sensors. *IEEE Trans. Geosci. Remote Sens.*, **34**, 1213–1232, https://doi.org/10.1109/36.536538.

——, and Coauthors, 2001: The evolution of the Goddard Profiling algorithm (GPROF) for rainfall estimation from passive microwave sensors. *J. Appl. Meteor.*, **40**, 1801–1820, https://doi.org/10.1175/1520-0450(2001)040<1801:TEOTGP>2.0.CO;2.

——, S. Ringerud, J. Crook, D. Randel, and W. Berg, 2011: An observationally generated a priori database for microwave rainfall retrievals. *J. Atmos. Oceanic Technol.*, **28**, 113–130, https://doi.org/10.1175/2010JTECHA1468.1.

——, D. L. Randel, M. Kulie, N. Y. Wang, R. Ferraro, S. J. Munchak, and V. Petkovic, 2015: The evolution of the Goddard profiling algorithm to a fully parametric scheme. *J. Atmos. Oceanic Technol.*, **32**, 2265–2280, https://doi.org/10.1175/JTECH-D-15-0039.1.

Kunkel, K. E., N. E. Westcott, and D. A. R. Kristovich, 2002: Assessment of potential effects of climate change on heavy lake-effect snowstorms near Lake Erie. *J. Great Lakes Res.*, **28**, 521–536, https://doi.org/10.1016/S0380-1330(02)70603-5.

Liu, A. Q., and G. W. K. Moore, 2004: Lake-effect snowstorms over southern Ontario, Canada, and their associated synoptic-scale environment. *Mon. Wea. Rev.*, **132**, 2595–2609, https://doi.org/10.1175/MWR2796.1.

Liu, G., and E.-K. Seo, 2013: Detecting snowfall over land by satellite high-frequency microwave observations: The lack of scattering signature and a statistical approach. *J. Geophys. Res. Atmos.*, **118**, 1376–1387, https://doi.org/10.1002/jgrd.50172.

Maahn, M., C. Burgard, S. Crewell, I. V. Gorodetskaya, S. Kneifel, S. Lhermitte, K. Van Tricht, and N. P. M. van Lipzig, 2014: How does the spaceborne radar blind zone affect derived surface snowfall statistics in polar regions? *J. Geophys. Res. Atmos.*, **119**, 13 604–13 620, https://doi.org/10.1002/2014JD022079.

Meng, H., J. Dong, R. Ferraro, B. Yan, L. Zhao, C. Kongoli, N.-Y. Wang, and B. Zavodsky, 2017: A 1DVAR-based snowfall rate retrieval algorithm for passive microwave radiometers. *J. Geophys. Res.*, **122**, 6520–6540, https://doi.org/10.1002/2016JD026325.

Meyers, P. C., R. R. Ferraro, and N. Y. Wang, 2015: Updated screening procedures for GPROF2010 over land: Utilization for AMSR-E. *J. Atmos. Oceanic Technol.*, **32**, 1015–1028, https://doi.org/10.1175/JTECH-D-14-00149.1.

Munchak, S. J., S. Ringerud, L. Brucker, Y. You I. Gelis, and C. Prigent, 2020: An active-passive microwave land surface database from GPM. *IEEE Trans. Geosci. Remote Sens.*, **58**, 6224–6242, https://doi.org/10.1109/TGRS.2020.2975477.

Notaro, M., A. Zarrin, S. Vavrus, and V. Bennington, 2013: Simulation of heavy lake-effect snowstorms across the Great Lakes Basin by RegCM4: Synoptic climatology and variability. *Mon. Wea. Rev.*, **141**, 1990–2014, https://doi.org/10.1175/MWR-D-11-00369.1.

Nurmi, P., 2003: Recommendations on the verification of local weather forecasts. ECMWF Tech. Memo. 430, 19 pp., https://doi.org/10.21957/y1z1thg5l.

NWS, 2019: National snow analysis. National Operational Hydrologic Remote Sensing Center, accessed 25 November 2020, https://www.nohrsc.noaa.gov/nsa/.

——, 2020: Lake effect snow event archive. NWS Forecast Office, Buffalo, NY, accessed 25 November 2020, https://www.weather.gov/buf/lesEventArchive?season=2019-2020&event=A.

Panegrossi, G., J.-F. Rysman, D. Casella, A. Marra, P. Sanò, and M. Kulie, 2017: CloudSat-based assessment of GPM microwave imager snowfall observation capabilities. *Remote Sens.*, **9**, 1263, https://doi.org/10.3390/rs9121263.

Passive Microwave Algorithm Team Facility, 2017: GPROF2017, version 1 (used in GPM V5 processing). Global Precipitation Measurement (GPM) Mission Algorithm Theoretical Basis Doc., 63 pp., https://pmm.nasa.gov/sites/default/files/document_files/ATBD_GPM_GPROF_June1_2017.pdf.

Petersen, W. A., P.-E. Kirstetter, J. Wang, D. B. Wolff, and A. Tokay, 2020: The GPM ground validation program. *Satellite Precipitation Measurement*, V. Levizzani et al., Eds., Advances in Global Change Research, Vol. 69, Springer Nature, 471–502.

Pettersen, C., R. Bennartz, A. J. Merrelli, M. D. Shupe, D. D. Turner, and V. P. Walden, 2018: Precipitation regimes over central Greenland inferred from 5 years of ICECAPS observations. *Atmos. Chem. Phys.*, **18**, 4715–4735, https://doi.org/10.5194/acp-18-4715-2018.

——, M. S. Kulie, L. F. Bliven, A. J. Merrelli, W. A. Petersen, T. J. Wagner, D. B. Wolff, and N. B. Wood, 2020: A composite analysis of snowfall modes from four winter seasons in Marquette, Michigan. *J. Appl. Meteor. Climatol.*, **59**, 103–124, https://doi.org/10.1175/JAMC-D-19-0099.1.

Prigent, C., F. Aires, and W. B. Rossow, 2006: Land surface microwave emissivities over the globe for a decade. *Bull. Amer. Meteor. Soc.*, **87**, 1573–1584, https://doi.org/10.1175/BAMS-87-11-1573.

Reed, P. M., N. W. Chaney, J. D. Herman, M. P. Ferringer, and E. F. Wood, 2015: Internationally coordinated multi-mission planning is now critical to sustain the space-based rainfall observations needed for managing floods globally. *Environ. Res. Lett.*, **10**, 024010, https://doi.org/10.1088/1748-9326/10/2/024010.

Rodgers, C. D., 2000: *Inverse Methods for Atmospheric Sounding: Theory and Practice*. World Scientific, 238 pp.

Romanov, P., G. Gutman, and I. Csiszar, 2000: Automated monitoring of snow cover over North America with multispectral satellite data. *J. Appl. Meteor.*, **39**, 1866–1880, https://doi.org/10.1175/1520-0450(2000)039<1866:AMOSCO>2.0.CO;2.

Rysman, J.-F., G. Panegrossi, P. Sanò, A. Marra, S. Dietrich, L. Milani, and M. Kulie, 2018: SLALOM: An all-surface snow water path retrieval algorithm for the GPM Microwave Imager. *Remote Sens.*, **10**, 1278, https://doi.org/10.3390/rs10081278.

——, and Coauthors, 2019: Retrieving surface snowfall with the GPM microwave imager: A new module for the SLALOM algorithm. *Geophys. Res. Lett.*, **46**, 13 593–13 601, https://doi.org/10.1029/2019GL084576.

Scott, R. W., and F. A. Huff, 1996: Impacts of the Great Lakes on regional climate conditions. *J. Great Lakes Res.*, **22**, 845–863, https://doi.org/10.1016/S0380-1330(96)71006-7.

Sims, E. M., and G. Liu, 2015: A parameterization of the probability of snow–rain transition. *J. Hydrometeor.*, **16**, 1466–1477, https://doi.org/10.1175/JHM-D-14-0211.1.

Skofronick-Jackson, G., and B. T. Johnson, 2011: Surface and atmospheric contributions to passive microwave brightness temperatures for falling snow events. *J. Geophys. Res.*, **116**, D02213, https://doi.org/10.1029/2010JD014438.

——, M. J. Kim, J. A. Weinman, and D. E. Chang, 2004: A physical model to determine snowfall over land by microwave radiometry. *IEEE Trans. Geosci. Remote Sens.*, **42**, 1047–1058, https://doi.org/10.1109/TGRS.2004.825585.

——, B. T. Johnson, and S. J. Munchak, 2013: Detection thresholds of falling snow from satellite-borne active and passive sensors. *IEEE Trans. Geosci. Remote Sens.*, **51**, 4177–4189, https://doi.org/10.1109/TGRS.2012.2227763.

——, and Coauthors, 2017: The Global Precipitation Measurement (GPM) mission for science and society. *Bull. Amer. Meteor. Soc.*, **98**, 1679–1695, https://doi.org/10.1175/BAMS-D-15-00306.1.

——, M. Kulie, L. Milani, S. J. Munchak, N. B. Wood, and V. Levizzani, 2019: Satellite estimation of falling snow: A Global Precipitation Measurement (GPM) *Core Observatory* perspective. *J. Appl. Meteor. Climatol.*, **58**, 1429–1448, https://doi.org/10.1175/JAMC-D-18-0124.1.

Sorooshian, S., and Coauthors, 2011: Advancing the remote sensing of precipitation. *Bull. Amer. Meteor. Soc.*, **92**, 1271–1272, https://doi.org/10.1175/BAMS-D-11-00116.1.

Steiger, S. M., and Coauthors, 2013: Circulations, bounded weak echo regions, and horizontal vortices observed within long-lake-axis-parallel–lake-effect storms by the Doppler on wheels. *Mon. Wea. Rev.*, **141**, 2821–2840, https://doi.org/10.1175/MWR-D-12-00226.1.

Tang, G., M. P. Clark, S. M. Papalexiou, Z. Ma, and Y. Hong, 2020: Have satellite precipitation products improved over last two decades? A comprehensive comparison of GPM IMERG with nine satellite and reanalysis datasets. *Remote Sens. Environ.*, **240**, 111697, https://doi.org/10.1016/j.rse.2020.111697.

Toyoshima, K., H. Masunaga, and F. A. Furuzawa, 2015: Early evaluation of Ku- and Ka-band sensitivities for the Global Precipitation Measurement (GPM) Dual-Frequency Precipitation Radar (DPR). *SOLA*, **11**, 14–17, https://doi.org/10.2151/sola.2015-004.

Turk, F. J., 2016: CloudSat-GPM coincidence dataset. NASA, accessed 25 November 2020, https://gpm.nasa.gov/sites/default/files/document_files/CSATGPM_COIN_ATBD.pdf.

——, Z. S. Haddad, P.-E. Kirstetter, Y. You, and S. Ringerud, 2018: An observationally based method for stratifying a priori passive microwave observations in a Bayesian-based precipitation retrieval framework. *Quart. J. Roy. Meteor. Soc.*, **144**, 145–164, https://doi.org/10.1002/qj.3203.

Wentz, F. J., and D. Draper, 2016: On-orbit absolute calibration of the global precipitation measurement microwave imager. *J. Atmos. Oceanic Technol.*, **33**, 1393–1412, https://doi.org/10.1175/JTECH-D-15-0212.1.

West, T. K., W. J. Steenburgh, and G. G. Mace, 2019: Characteristics of sea-effect clouds and precipitation over the Sea of Japan region as observed by the A-Train satellites. *J. Geophys. Res. Atmos.*, **124**, 1322–1335, https://doi.org/10.1029/2018JD029586.

You, Y., N.-Y. Wang, R. Ferraro, and S. Rudlosky, 2017: Quantifying the snowfall detection performance of the GPM Microwave Imager channels over land. *J. Hydrometeor.*, **18**, 729–751, https://doi.org/10.1175/JHM-D-16-0190.1.

Zhang, J., and Coauthors, 2011: National Mosaic and Multi-Sensor QPE (NMQ) system: Description, results, and future plans. *Bull. Amer. Meteor. Soc.*, **92**, 1321–1338, https://doi.org/10.1175/2011BAMS-D-11-00047.1.